The Nature of Optical Afterglows without Gamma-Ray Bursts: Identification of AT2023lcr and Multiwavelength Modeling

Maggie L. Li[1,2] , Anna Y. Q. Ho[1] , Geoffrey Ryan[3] , Daniel A. Perley[4] , Gavin P. Lamb[4] , Nayana A.J.[5] ,
Igor Andreoni[6,7,8,9] , G. C. Anupama[10] , Eric C. Bellm[11] , Edo Berger[12] , Joshua S. Bloom[13,14] , Eric Burns[15] ,
Ilaria Caiazzo[2] , Poonam Chandra[16] , Michael W. Coughlin[17] , Kareem El-Badry[2] , Matthew J. Graham[2] ,
Mansi Kasliwal[2] , Garrett K. Keating[12] , S. R. Kulkarni[2] , Harsh Kumar[12,18,19] , Frank J. Masci[20] , Richard A. Perley[21] ,
Josiah Purdum[22] , Ramprasad Rao[12] , Antonio C. Rodriguez[2] , Ben Rusholme[20] , Nikhil Sarin[23,24] , Jesper Sollerman[25] ,
Gokul P. Srinivasaragavan[6,7,8] , Vishwajeet Swain[26] , and Zachary Vanderbosch[2]
[1] Department of Astronomy, Cornell University, Ithaca, NY 14853, USA; mll285@cornell.edu
[2] Cahill Center for Astrophysics, California Institute of Technology, MC 249-17, 1200 E California Boulevard, Pasadena, CA 91125, USA
[3] Perimeter Institute for Theoretical Physics, Waterloo, Ontario N2L 2Y5, Canada
[4] Astrophysics Research Institute, Liverpool John Moores University, IC 2, Liverpool Science Park, 146 Brownlow Hill, Liverpool L3 5RF, UK
[5] National Centre for Radio Astrophysics, Tata Institute of Fundamental Research, Pune University Campus, Ganeshkhind Pune 411007, India
[6] Joint Space-Science Institute, University of Maryland, College Park, MD 20742, USA
[7] Department of Astronomy, University of Maryland, College Park, MD 20742, USA
[8] Astrophysics Science Division, NASA Goddard Space Flight Center, 8800 Greenbelt Road, Greenbelt, MD 20771, USA
[9] University of North Carolina at Chapel Hill, 120 E. Cameron Avenue, Chapel Hill, NC 27514, USA
[10] Indian Institute of Astrophysics, II Block Koramangala, Bengaluru 560034, India
[11] DIRAC Institute, Department of Astronomy, University of Washington, 3910 15th Avenue NE, Seattle, WA 98195, USA
[12] Center for Astrophysics | Harvard & Smithsonian, 60 Garden Street, Cambridge, MA 02138-1516, USA
[13] Department of Astronomy, University of California, Berkeley, CA 94720, USA
[14] Physics Division, Lawrence Berkeley National Laboratory, 1 Cyclotron Road, MS 50B-4206, Berkeley, CA 94720, USA
[15] Department of Physics & Astronomy, Louisiana State University, Baton Rouge, LA 70803, USA
[16] National Radio Astronomy Observatory, 520 Edgemont Road, Charlottesville, VA 22903, USA
[17] School of Physics and Astronomy, University of Minnesota, Minneapolis, MN 55455, USA
[18] Physics Department, Indian Institute of Technology Bombay, Powai, 400 076, India
[19] The NSF AI Institute for Artificial Intelligence and Fundamental Interactions, USA
[20] IPAC, California Institute of Technology, 1200 E. California Boulevard, Pasadena, CA 91125, USA
[21] National Radio Astronomy Observatory, PO Box 0, Socorro, NM 87801, USA
[22] Caltech Optical Observatories, California Institute of Technology, Pasadena, CA 91125, USA
[23] Nordita, Stockholm University and KTH Royal Institute of Technology, Hannes Alfvens vag 12, SE-106 91 Stockholm, Sweden
[24] Oskar Klein Centre for Cosmoparticle Physics, Department of Physics, Stockholm University, AlbaNova, Stockholm SE-106 91, Sweden
[25] Oskar Klein Centre, Department of Astronomy, Stockholm University, AlbaNova, SE-10691 Stockholm, Sweden
[26] Department of Physics, Indian Institute of Technology Bombay, Powai, 400 076, India

Abstract

In the past few years, the improved sensitivity and cadence of wide-field optical surveys have enabled the discovery of several afterglows without associated detected gamma-ray bursts (GRBs). We present the identification, observations, and multiwavelength modeling of a recent such afterglow (AT 2023lcr), and model three literature events (AT 2020blt, AT 2021any, and AT 2021lfa) in a consistent fashion. For each event, we consider the following possibilities as to why a GRB was not observed: (1) the jet was off-axis; (2) the jet had a low initial Lorentz factor; and (3) the afterglow was the result of an on-axis classical GRB (on-axis jet with physical parameters typical of the GRB population), but the emission was undetected by gamma-ray satellites. We estimate all physical parameters using `afterglowpy` and Markov Chain Monte Carlo methods from `emcee`. We find that AT 2023lcr, AT 2020blt, and AT 2021any are consistent with on-axis classical GRBs, and AT 2021lfa is consistent with both on-axis low Lorentz factor ($\Gamma_0 \approx 5$–13) and off-axis ($\theta_{\rm obs} = 2\theta_{\rm jet}$) high Lorentz factor ($\Gamma_0 \approx 100$) jets.

1. Introduction

In the internal-external shocks model for long-duration gamma-ray bursts (LGRBs; T. Piran 2005; P. Mészáros 2006; P. Kumar & B. Zhang 2015), the core of a massive star collapses and forms a neutron star or black hole, which launches an ultrarelativistic collimated outflow, or "jet." The jet's internal collisions produce an initial burst of gamma-rays, called the "prompt emission," followed by the jet's external collision with the ambient medium, producing an "afterglow" across the electromagnetic spectrum.

There are several reasons why we should be able to detect afterglows without associated detected gamma-ray bursts (GRBs). First, the Earth might not be within the jet's opening angle (typically $\theta_c = 5°$–$10°$; G. Ghirlanda et al. 2018), which is collimated and relativistically beamed (initial $\theta_c = \Gamma_0^{-1}$; T. Totani & A. Panaitescu 2002). In this "off-axis" GRB scenario, we will miss the prompt emission but still be able to observe an afterglow when the jet decelerates and spreads (J. E. Rhoads 1997). Second,

Table 1
Summary of Afterglows Discovered without Associated Detected GRBs

Afterglow	Redshift	References	Proposed Models
PTF 11agg	…	[1]	on-axis, untriggered GRB [1]; dirty fireball [1]; neutron star merger [2, 3]
AT 2019pim	1.2596	[4]	on-axis jet with $\Gamma_0 \approx 30$–50; off-axis GRB with $\Gamma_0 \approx 100$ [4]
AT 2020blt	2.9	[5]	on-axis GRB with $\eta_\gamma < 0.3$–14.5% [6]; on-axis classical GRB [0]
AT 2021any	2.5131	[7]	on-axis classical GRB [8; 0]; on-axis moderately dirty fireball [9; 0]
AT 2021lfa	1.063	[7, 10]	on-axis jet with $\Gamma_0 \sim 20$ [10, 11, 0]; off-axis GRB with $\Gamma_0 \approx 100$ [0]
AT 2023avj	…	[12, 13]	…
AT 2023azs	…	[14, 15]	…
AT 2023jxk	…	[16, 17]	…
AT 2023lcr	1.0272	[0]	on-axis GRB with $\eta_\gamma < 0.95\%$ [0]
AT 2023sva	2.281	[18, 19, 20, 21]	slightly off-axis, shallow structured jet [22]

References. [0] this work, [1] S. B. Cenko et al. (2013), [2] L.-J. Wang & Z.-G. Dai (2013), [3] X.-F. Wu et al. (2013), [4] D. A. Perley et al. (2025), [5] A. Y. Q. Ho et al. (2020), [6] N. Sarin et al. (2022), [7] A. Y. Q. Ho et al. (2022), [8] R. Gupta et al. (2022), [9] F. Xu et al. (2023), [10] V. Lipunov et al. (2022), [11] X.-M. Ye et al. (2024), [12] K. Wang et al. (2023), [13] A. Y. Q. Ho (2023), [14] I. Andreoni et al. (2023), [15] D. A. Perley (2023), [16] J. Vail et al. (2023a), [17] I. Sfaradi et al. (2023), [18] J. L. Vail et al. (2023b), [19] A. de Ugarte Postigo et al. (2023), [20] L. Rhodes et al. (2023), [21] O. J. Roberts et al. (2023), [22] G. P. Srinivasaragavan et al. (2025).

a "dirty fireball" can occur if the outflow is less relativistic than that of a typical GRB ($\Gamma_0 \lesssim 100$) due to a baryon-loaded jet (C. D. Dermer et al. 1999; Y. F. Huang et al. 2002; J. E. Rhoads 2003). In this case, the jet will be below the pair-production threshold for gamma-rays (i.e., the compactness problem; M. Ruderman 1975), so we would not be able to observe a GRB. Still, we might observe a less-energetic prompt emission, such as an X-ray flash (C. D. Dermer et al. 1999; J. Heise et al. 2001; W. Zhang et al. 2004; T. Sakamoto et al. 2005; A. M. Soderberg et al. 2007). Third, the source could be an on-axis classical GRB whose prompt emission was undetected by gamma-ray satellites, possibly due to the occultation of the Earth or a weak prompt emission that failed to meet the triggering thresholds of gamma-ray satellites.

In recent years, high-cadence optical surveys have enabled the discovery of 10 likely afterglows without associated detected GRBs, summarized in Table 1. Prior to the Zwicky Transient Facility (ZTF; E. C. Bellm et al. 2019a, 2019b; M. J. Graham et al. 2019; F. J. Masci et al. 2019; R. Dekany et al. 2020), only one such event, PTF 11agg (S. B. Cenko et al. 2013), was discovered, found by the Palomar Transient Factory (N. M. Law et al. 2009). Since ZTF's first light, nine other events have been confirmed as afterglows without associated detected GRBs, largely thanks to ZTF's high cadence over a wide field of view, enabling the rapid identification of fast transients. Still, no convincing dirty fireballs or off-axis LGRB candidates have been discovered.

In this paper, we present the identification, follow-up, and multiwavelength modeling of one of the most recent such events, AT 2023lcr. We only consider the afterglow light curve, although an associated Ic-BL supernova was identified at a later time (A. Martin-Carrillo et al. 2023a). As shown in Table 1, AT 2023lcr is one of six afterglows discovered in optical-survey data with no detected GRB but with a measured redshift. To put our AT 2023lcr results into context, we also present multiwavelength modeling of three afterglows in Table 1: AT 2020blt, AT 2021any, and AT 2021lfa. For AT 2019pim and AT 2023sva, we refer the reader to D. A. Perley et al. (2025) and G. P. Srinivasaragavan et al. (2025), who used similar approaches to this work. All afterglows are modeled using Markov Chain Monte Carlo (MCMC) methods in emcee (version 3.1.4; D. Foreman-Mackey et al.

2013) and afterglow models from afterglowpy (version 0.7.3; G. Ryan et al. 2020).

For each object, we consider the following explanations for why their prompt gamma-ray emission was missed: (1) the jet was off-axis; (2) the jet had a low Lorentz factor ($\Gamma_0 \lesssim 100$); and (3) the afterglow was the result of an on-axis classical GRB, but the GRB was undetected by high-energy satellites. Because of imprecise constraints on the burst time, the possibility of an on-axis classical GRB cannot be ruled out for any of the afterglows on the basis of gamma-ray limits alone (A. Y. Q. Ho et al. 2020, 2022).

AT 2020blt was previously modeled in N. Sarin et al. (2022, hereafter S22); AT 2021any was previously modeled in R. Gupta et al. (2022, hereafter G22) and F. Xu et al. (2023, hereafter X23); and AT 2021lfa was previously modeled in X.-M. Ye et al. (2024, hereafter Y24). In this work, we explore additional jet structures, modeling configurations, and constraints on afterglow behavior, discussing comparisons between the mentioned works and this work in Section 5.

This paper is organized as follows: we present observations of AT 2023lcr in Section 2. We describe observational features of AT 2023lcr in Section 3. We describe our fitting framework in Section 4. In Section 5, we present the results of our fitting, discuss preferred models and physical interpretations, and compare our results to past works. Finally, we summarize and discuss implications and future work in Section 6.

2. AT2023lcr Observations

2.1. Optical Photometry

AT 2023lcr was initially reported (J. Tonry et al. 2023; M. D. Fulton et al. 2023) to the Transient Name Server by the ATLAS survey (J. L. Tonry et al. 2018) as ATLAS23msn. AT 2023lcr was also detected as part of the ZTF high-cadence partnership survey (E. C. Bellm et al. 2019b), with the first detection at[27] 06:36:27 on 2023 June 18 (internal name ZTF23aaoohpy) at a position $\alpha = 16:31:37.416$ and $\delta = +26:21:58.31$ (J2000) and a Galactic latitude $b = 41.25$ deg (V. Swain et al. 2023a). AT 2023lcr was flagged as a transient

---

[27] All times in this paper are in UT.
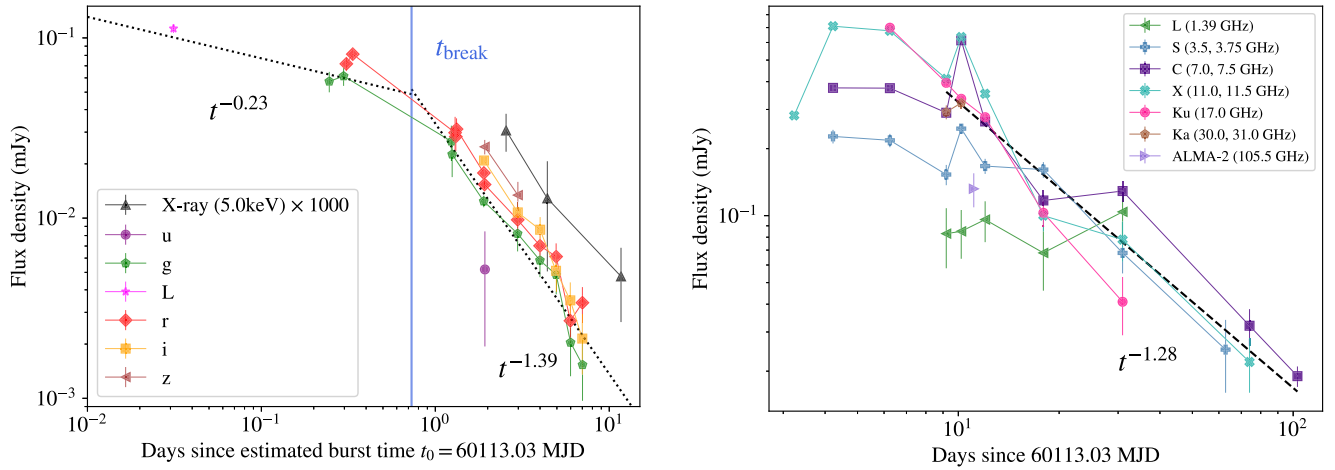
Figure 1. Left panel: the optical light curve of AT 2023lcr with the best-fit broken power law to g-, r-, i-, and z-band observations. The vertical line marks the best-fit break time. Right panel: the radio light curve of AT 2023lcr with the best-fit power law to all bands shown. For each band, we select a frequency with observations in the most number of epochs. The early radio emission is likely impacted by interstellar scintillation.

of interest due to its rapid rise (>1.2 mag day^{-1} in r band[28]), red colors ($g-r = 0.29 \pm 0.08$ mag, corrected for Milky Way extinction with $E(B - V) = A_V/R_V = 0.05$, assuming $R_v = 3.1$; D. J. Schlegel et al. 1998), and lack of a bright host-galaxy counterpart.

The red colors exhibited by AT 2023lcr were consistent with the synchrotron emission expected from an afterglow-like transient, which has been shown to be a useful discriminant from stellar flares in the Milky Way (A. Y. Q. Ho et al. 2020). Liverpool Telescope (LT; I. A. Steele et al. 2004) IO:O imaging observations were attempted to confirm the synchrotron-like colors and check for rapid fading (as expected for an afterglow) but the telescope was offline due to a power supply problem. Confirmation of the red colors and rapid fading was obtained by ZTF through routine survey operations the following night: the transient faded by approximately one magnitude in both the g and r band, and this behavior was flagged (V. Swain et al. 2023b) by the ZTFReST pipeline (I. Andreoni et al. 2021).

The Gravitational-wave Optical Transient Observer (GOTO; D. Steeghs et al. 2022) reported (B. Gompertz et al. 2023) an early detection of AT 2023lcr at 01:27:41 on 2023 June 18 (60113.06089 MJD), 5 hr before the first ZTF detection, at 18.77 ± 0.06 in the L band (400–700 nm). It was not detected in the previous GOTO epoch at 23:50:30 on 2023 June 17 with a 5σ limiting magnitude of $L > 20.3$ mag, establishing a short window for the onset time of 1 hr and 38 minutes.

Optical photometric follow-up observations were obtained during the week following the initial detection. Table 15 in Appendix 15 presents the LT, GROWTH-India Telescope (GIT), and Himalayan Chandra Telescope (HCT) photometry. To correct for Milky Way extinction, we use $A_V = 0.128$ mag (E. F. Schlafly & D. P. Finkbeiner 2011). The full optical light curve of AT 2023lcr is shown in Figure 1. Follow-up observations were coordinated using the SkyPortal platform (S. van der Walt et al. 2019; M. W. Coughlin et al. 2023).

Later, on 2023 August 12, a James Webb Space Telescope/ NIRSPec spectrum was taken (A. Martin-Carrillo et al. 2023b), which identified a Ic-BL supernova (SN) counterpart for AT 2023lcr. In this work, we only consider the afterglow. Since

the source is at a redshift $z = 1.0272$, we assume that the contribution of the SN is negligible in our observations, supported by the lack of observed flattening in the optical light curve.

2.2. Optical Spectroscopy

We triggered observations[29] using the Low Resolution Imaging Spectrometer (LRIS; J. B. Oke et al. 1995) on the Keck I 10 m telescope. Observations started at 07:22 on 2023 June 20 ($\Delta t = 2.3$ days from the last GOTO nondetection[30,31]), with exposure times of 2×1200 s and 3×800 s in the blue and red arms, respectively. Observations employed the 600/ 4000 blue grism and 600/7500 red grating, providing continuous wavelength coverage from 3140 to 8784 Å. Data were reduced using LPipe (D. A. Perley 2019). The spectrum (Figure 2) shows a simple continuum, well fit by a power law of $f_\lambda \propto \lambda^{-1}$. The signal-to-noise ratio is about 20 per resolution element (although lower blueward of 4000 Å). We detect clear (but weak) absorption lines at observer-frame wavelengths of 5688 and 5683 Å, which we attribute to redshifted Mg II$\lambda\lambda$2796, 2803 at $z = 1.0272$. Weak absorption from Fe IIλ2383 and Fe IIλ2600 at a consistent redshift is also securely detected, and Fe IIλ2344 is marginally detected. We also detect a possible intervening Mg II absorber at $z = 0.7795$. No other lines are apparent in the spectrum. Based on this information, we adopt $z = 1.0272$ as the redshift of AT 2023lcr, and the corresponding luminosity distance[32] as $D_L = 7.0196$ Gpc. While strictly this redshift is only a lower limit, the absence of any higher-redshift absorption features suggests that a higher-redshift origin is unlikely. The lack of Lyman-α absorption over the spectral range imposes a redshift upper limit of $z < 1.6$.

2.3. X-Rays

We triggered observations of AT 2023lcr with the X-ray Telescope (XRT; D. N. Burrows et al. 2005) on board the Neil

---

[28] All magnitudes are in AB unless specified otherwise.

[29] PI K. El-Badry.
[30] In this work, Δt is the observer-frame time in days since the afterglow's last nondetection, unless specified otherwise. For AT 2023lcr, the last GOTO nondetection was at 60112.99340 MJD.
[31] In this work, all times are observer-frame unless specified otherwise.
[32] ΛCDM cosmology of Planck Collaboration et al. (2020) is used throughout.
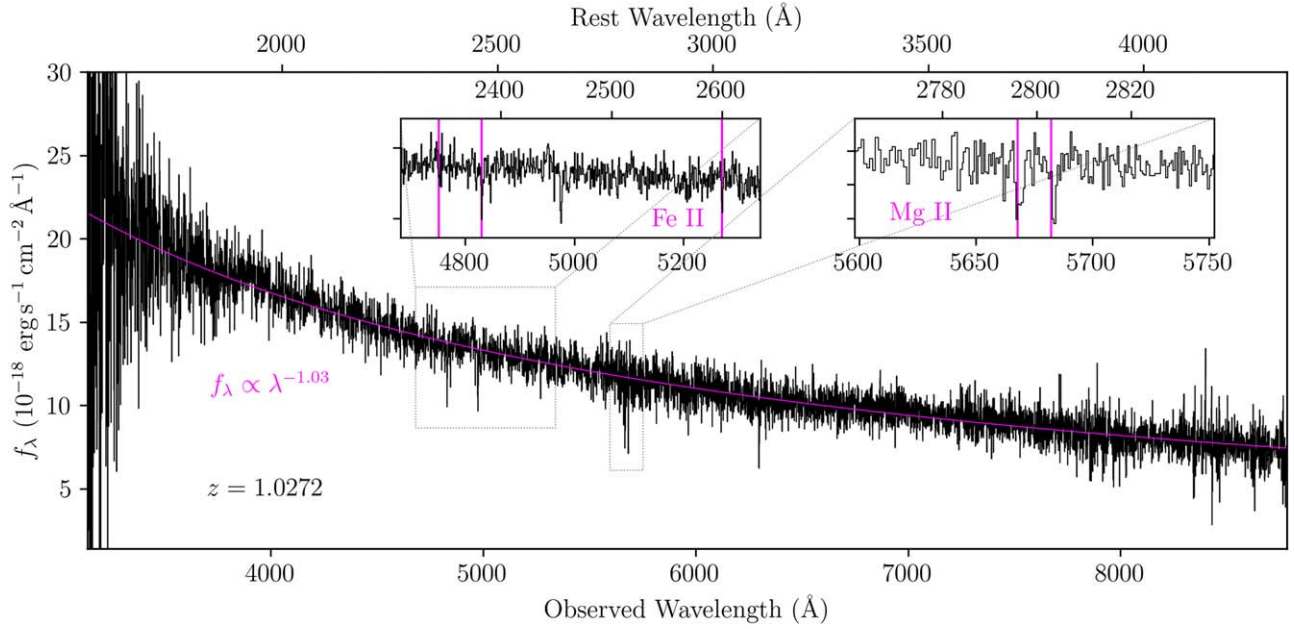
Figure 2. Keck/LRIS spectrum of AT 2023lcr, with the best-fit power-law index shown as a solid line. The insets show zoom-ins of the regions used to measure the redshift.

Table 2
0.3–10 keV X-Ray Observations AT 2023lcr

Instrument	Start Date (MJD)	Exposure Time (ks)	Flux (10^{-13} erg s^{-1} cm^{-2})	f_ν (1 keV; 10^{-2} μJy)
Swift/XRT	60115.58090	3.00	$3.70^{+0.88}_{-0.88}$	$4.40^{+1.05}_{-1.05}$
Swift/XRT	60117.43457	3.30	$1.56^{+0.94}_{-0.70}$	$1.85^{+1.12}_{-0.83}$
Swift/XRT	60124.71261	9.10	$0.57^{+0.25}_{-0.21}$	$0.68^{+0.30}_{-0.24}$
Chandra/ACIS	60128.27391	18.83	$0.28^{+0.10}_{-0.05}$	$0.33^{+0.11}_{-0.06}$

Note. Uncertainties are 68%.

Gehrels Swift Observatory through SkyPortal (S. van der Walt et al. 2019; M. W. Coughlin et al. 2023). In total, six epochs of observations were obtained under target-of-opportunity programs,[33] from 2023 June 20 to 2023 July 6 ($\Delta t = $ 2–18 days). The source was detected in three of those epochs, presented in Table 2. Fitting the detections in the three epochs simultaneously using the Swift tool (P. A. Evans et al. 2007; P. A. Evans et al. 2009), with a Galactic hydrogen column density of $N_H = 4.12 \times 10^{20}$ cm^{-2}, we find a best-fit photon index of $\Gamma = 1.8^{+0.8}_{-0.5}$ (90% confidence interval). To convert from count rate to flux density, we take $\Gamma = 2$, giving a counts to flux conversion factor (unabsorbed) of 3.93×10^{-11} erg cm^{-2} ct^{-1}. This photon index corresponds to a spectral index of $\beta_X = 1 - \Gamma = -1$ where $f_\nu \propto \nu^{\beta_X}$.

AT 2023lcr was also observed by the Advanced CCD imaging spectrometer (ACIS; G. P. Garmire et al. 2003) on board the Chandra X-Ray Observatory (Chandra) [34] under a Director's Discretionary Time proposal,[35] 4 days after the final Swift/XRT detection. We reduced the data using the Chandra Interactive Analysis of Observations (CIAO; A. Fruscione et al. 2006) software package (v4.15). Counts were extracted from AT 2023lcr using a circle with radius 2″, and background

counts were measured in source-free regions near AT 2023lcr. We used specextract to bin the spectrum (with 5 counts per bin). The routine sherpa (P. Freeman et al. 2001; S. Doe et al. 2007) was used to fit the spectrum in the range 0.5–6 keV, with the background subtracted, using a model with photo-electric absorption and a single-component power law (xsphabs.abs1 × powlaw1d.p1). We set the Galactic hydrogen column density to be the same as for the *Swift* observations. The best-fit power-law index was $\Gamma = 1.16^{+0.95}_{-0.95}$ (68% confidence), consistent with the value from Swift but with much larger uncertainties; so for consistency, we also adopt $\Gamma = 2$. The flux reported in Table 2 has been multiplied by a factor of 1.77 to correct from the 0.5–6 keV band to the 0.3–10 keV band. In Table 2, we also present the spectral flux density at 1 keV assuming a spectral index of $f_\nu \propto \nu^{-1}$.

2.4. Radio

We obtained 11 epochs of observations using the Karl G. Jansky Very Large Array (VLA[36]; R. A. Perley et al. 2011.), spanning 2023 June 21 to 2023 September 29 ($\Delta t = $ 3–103 days) in the *L, S, C, X, Ku,* and *Ka* bands (1–40 GHz). The primary flux calibrator used was 3C286. Data were calibrated and imaged using standard procedures in the Astronomical Image Processing System. Images were typically made in separate windows

---

[33] TOO IDs 18987 and 18992, PIs M. Coughlin and D. Malesani.
[34] This paper employs a list of Chandra data sets, obtained by the Chandra X-ray Observatory, contained in Chandra Data Collection doi:10.25574/cdc.364.
[35] Proposal No. 24508916, PI A. Martin-Carrillo.

[36] Program IDs 23A-355 and 23A-426, PI D. Perley.

with a bandwidth of 1 GHz or 2 GHz, with adjustments made at lower frequencies due to radio frequency interference excision. Flux-density measurements were performed using `jmfit`. The second *Ka*-band epoch was hampered by poor weather conditions, resulting in poor phase stability (with insufficient signal to noise for self-calibration); this measurement should be regarded as a lower limit. Epoch 9 on 2023 August 19 ($\Delta t = 62$ days) was also hampered by poor phase stability. For Epochs 4–8 ($\Delta t = 9$–31 days), we obtained *C*-band observations at the beginning and end of the block in order to search for scintillation.

We obtained observations on epochs 2023 June 29 ($\Delta t = 11$ days) and 2023 July 04 ($\Delta t = 16$ days) using the Atacama Large Millimeter/submillimeter Array (ALMA) under Director's Discretionary Time.[37] Weather conditions in both epochs were excellent. Data were calibrated and imaged using the automated CASA-based pipeline (CASA Team et al. 2022). Both observations were in Band 3 (100 GHz) and yielded a detection with a centroid position of $\alpha = $ 16:31:37.419, and $\delta = +26$:21:58.27 (J2000), consistent with the optical position. The peak flux density of the source was $140 \pm 14\,\mu$Jy in the first epoch and $94 \pm 11\,\mu$Jy in the second epoch.

We obtained one epoch of observations with the Submillimeter Array (SMA[38]) on 2023 June 24 ($\Delta t = 6$ days). Observations were conducted between 03:31 and 14:43 UT, using seven antennas, with an local oscillator frequency of 225.5 GHz. Weather conditions were favorable (median $\tau_{225\,\mathrm{GHz}} = 0.070$), with good phase stability for all but the first hour of observations. A total of 6.75 hr was spent on source, with 1613+342 and 3C345 used as gain calibrators, and Ceres as the flux calibrator. There was no detection.

We obtained Giant Metrewave Radio Telescope (GMRT) observations from 2023 August 9.63 UT to 2023 August 22.63 UT through a DDT proposal.[39] The observations were carried out in three frequency bands: band-5 (1000–1460 MHz), band-4 (550–850 MHz), and band-3 (250–500 MHz). The data were collected in standard continuum mode with a time integration of 10 s. We used a processing bandwidth of 400 MHz in band-5 and 200 MHz in bands-3 and 4, both split into 2048 channels. 3C286 was used as the flux density and bandpass calibrator, while J1609+266 was used as the phase calibrator. Emission was detected at 1.37 GHz, but not at 0.75 or 0.44 GHz.

All radio flux-density values are provided in Table 16 in Appendix B. The radio light curves are shown in Figure 1, and the evolution of the radio spectral energy distribution (SED) is shown in Figure 3.

2.5. Search for Gamma-Ray Emission

Throughout the 1 hr and 38 minutes between the last GOTO nondetection and the first GOTO detection, the KONUS instrument on the Wind spacecraft (R. L. Aptekar et al. 1995) was observing the entire sky, with no GRB detection. For a typical LGRB spectrum, the 90% confidence upper limit on the 20–1500 keV peak flux was reported to be $1.8 \times 10^{-7}\,\mathrm{erg\,cm^{-2}\,s^{-1}}$ on a 2.944 s scale (A. Ridnaia et al. 2023). At the redshift of AT 2023lcr ($z = 1.0272$), this corresponds to an upper limit on the isotropic-equivalent γ-ray luminosity of
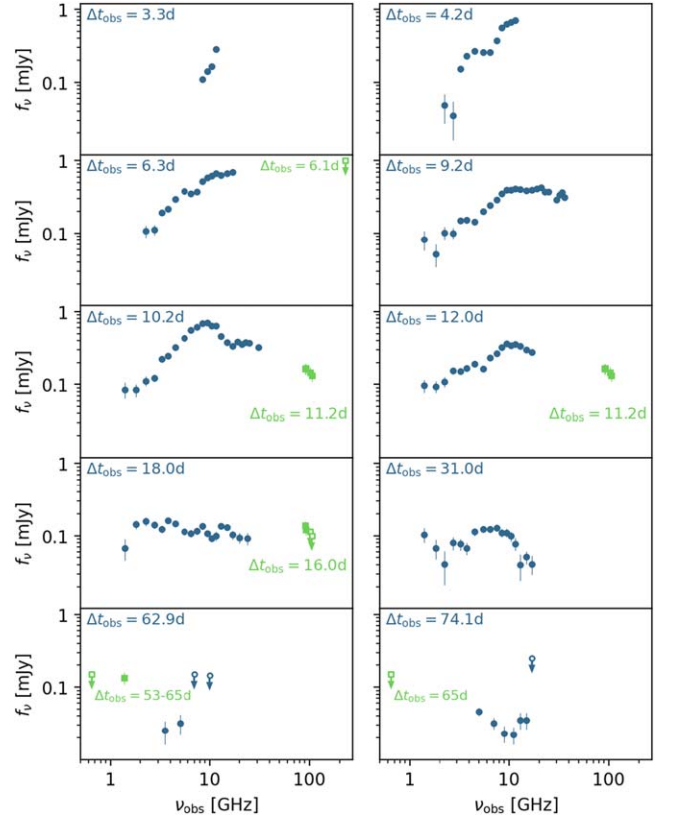
Figure 3. Evolution of the radio spectral energy distribution (SED) of AT 2023lcr. Upper limits (open symbols with arrows) are 5σ. VLA (ALMA, GMRT) data are shown as blue circles (green squares). Epochs are given in the observer frame. The *Ka*-band (30 GHz) observation at $\Delta t_{\mathrm{obs}} = 10.2$ days and observations at $\Delta t_{\mathrm{obs}} = 62.9$ days were impacted by bad weather.

$L_{\gamma,\mathrm{iso}} < 5.2 \times 10^{50}\,\mathrm{erg\,s^{-1}}$. Assuming a similar scaling over longer time intervals (an observed duration of 40 s, as in D. A. Perley et al. 2025) gives a limit on the isotropic-equivalent energy of $E_{\gamma,\mathrm{iso}} < 2.1 \times 10^{52}\,\mathrm{erg}$. We perform the same computation at the redshift upper limit of AT 2023lcr ($z = 1.6$), obtaining $L_{\gamma,\mathrm{iso}} < 1.2 \times 10^{51}\,\mathrm{erg\,s^{-1}}$ and $E_{\gamma,\mathrm{iso}} < 4.9 \times 10^{52}\,\mathrm{erg}$.

The position was visible to the Fermi Gamma-ray Burst Monitor (GBM; C. Meegan et al. 2009) for 1 hr, from 00:23:05 to 01:22:27 on 2023 June 18 with no South Atlantic Anomaly interruptions. A subthreshold search yielded no detections, with a mean upper limit on the peak flux (for the same burst duration) of $8.2 \times 10^{-8}\,\mathrm{erg\,cm^{-2}\,s^{-1}}$. This corresponds to $L_{\gamma,\mathrm{iso}} < 4.8 \times 10^{50}\,\mathrm{erg\,s^{-1}}$, or $E_{\gamma,\mathrm{iso}} < 9.5 \times 10^{51}\,\mathrm{erg}$. The position was visible to the Swift Burst Alert Telescope (BAT; S. D. Barthelmy et al. 2005) for 40 minutes, from approximately 00:38 to 01:20.

Given the incomplete coverage of both GBM and Swift BAT, we adopt the more conservative limit from KONUS in what follows.

3. Observational Features of AT2023lcr

We find preliminary radio, optical, and X-ray temporal indices for AT 2023lcr. We also compare AT 2023lcr's observational features to those of other $z \approx 1$ afterglows without associated detected GRBs, namely AT 2019pim at $z = 1.2596$ (D. A. Perley et al. 2025) and AT 2021lfa at $z = 1.0624$ (A. Y. Q. Ho et al. 2022).

3.1. Optical

We fit the multiband optical light curve of AT 2023lcr assuming a magnitude offset between each pair of bands that is constant over time, rather than a single overall spectral index. We treat the GOTO L-band point as the average of the r- and g-band fluxes at that time. We fit the g-, r-, i-, and z-band extinction-corrected light curves using the following smoothed broken power-law function (K. Beuermann et al. 1999; A. Zeh et al. 2006):

$$m(t) = m_c + \frac{2.5}{n} \log_{10}\left[\frac{(t-t_0)^{\alpha_1 n}}{t_b - t_0} + \frac{(t-t_0)^{\alpha_2 n}}{t_b - t_0} \right] \quad (1)$$

where $m(t)$ is the apparent magnitude as a function of time, n parameterizes the smoothness of the break ($n = \infty$ is a sharp break), α_1 and α_2 are the pre- and post-break temporal indices, respectively, t_0 is the time of the explosion in days, t_b is the time of the break in days, and m_c is the magnitude at the time of the break assuming $n = \infty$. We assume no contribution from the host galaxy or the underlying SN. A typical GRB-SN would be both too faint for our observations and redshifted to the NIR. These assumptions are supported by the lack of observed flattening in the optical light curve. We fixed $n = 2$ and allowed t_0 to vary between the time of the last GOTO nondetection and the first GOTO detection.

From an MCMC fit, we find (see left panel of Figure 1), a break time $t_b = 0.73^{+0.06}_{-0.06}$ days in the observer frame (68% confidence). The best-fit broken power-law temporal indices are $\alpha_1 = 0.23^{+0.04}_{-0.03}$ and $\alpha_2 = 1.39^{+0.05}_{-0.04}$. We find a best-fit t_0 that is 52^{+16}_{-18} minutes after the GOTO nondetection (and 45 minutes before the first GOTO detection), at MJD 60113.02965.

The optical light curve of AT 2023lcr is very similar to the early ($\Delta t < 10$ days) optical light curve of AT 2019pim, although the light curve of AT 2019pim was better resolved due to TESS coverage. From A. Y. Q. Ho et al. (2022), the optical light curve of AT 2021lfa had a much steeper temporal decay index than AT 2023lcr, $t^{-2.5}$ rather than t^{-1}, although we caution that the decay index is highly sensitive to the explosion time, which, for AT 2021lfa, is quite uncertain (1.79 days between the first detection and last nondetection). Using the burst time estimate obtained from results that follow in Section 5.1, AT 2021lfa returns a more similar temporal decay index $t^{-1.4}$.

Finally, to measure the spectral index across the optical bands, we use the ugriz photometry from LT in the MJD range 60114.92765–60114.95733 and apply a correction for Milky Way extinction. We find a best-fit spectral index of $\beta_{opt} = 1.20^{+0.16}_{-0.16}$ (68% confidence) where $f_\nu \propto \nu^{-\beta_{opt}}$, consistent with the spectral index measured from the optical spectrum (Figure 2). The spectral index from optical to X-ray bands, as well as within the X-ray band itself (Section 2.3), is also close to $f_\nu \propto \nu^{-1}$—this, together with the fairly smooth continuum observed in the spectrum, leads us to conclude that the impact of host-galaxy extinction is negligible.

3.2. X-Rays

We fit a single power law to the X-ray light curve of AT 2023lcr at 1 keV, and find a best-fit power-law index $\alpha_X = 1.47^{+0.17}_{-0.16}$ (68% confidence) where $f_\nu \propto t^{-\alpha_X}$, consistent with the slope of the optical light curve in the same time range. Given the similar optical and X-ray spectral indices ($f_\nu \propto \nu^{-1}$), we assume no host-galaxy extinction. There was only one X-ray
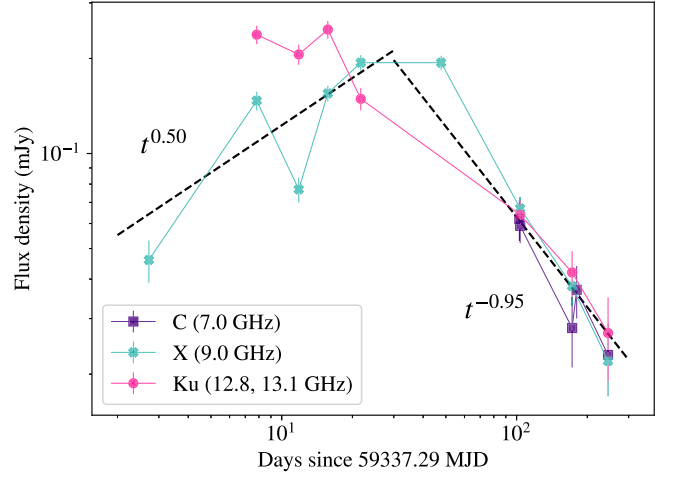
Figure 4. Radio temporal indices for AT 2021lfa. Indices and the estimated peak are highly affected by interstellar scintillation.

detection of AT 2021lfa, at a similar flux to AT 2023lcr. The X-ray light curves of AT 2023lcr and AT 2019pim have similar temporal decay indices, but the X-ray flux density of AT 2019pim was an order of magnitude fainter.

3.3. Radio

The radio light curves of AT 2019pim, AT 2021lfa, and AT 2023lcr reach a similar peak flux density and have roughly a single peak, rising $\sim t^1$ then decaying $\sim t^{-1.5}$, although AT 2021lfa's radio temporal indices are highly impacted by interstellar scintilation (see Figure 4 for the radio light curve fit of AT 2021lfa; see Figure 7 in D. A. Perley et al. 2025 for the radio light-curve fit of AT 2019pim). However, the peak for AT 2023lcr is at $t < 10$ days while the peak for AT 2019pim and AT 2021lfa is at tens of days. Additionally, AT 2023lcr, AT 2021lfa, and AT 2019pim all exhibit significant scintillation at $\nu \lesssim 10$ GHz. AT 2023lcr and AT 2019pim show evidence of scintillation until at least $\Delta t \approx 30$ days, but AT 2021lfa exhibits scintillation for much longer, until at least $\Delta t \approx 100$ days. The SED evolution is also similar among the three objects, with a hint of self-absorption in the first few days, and a broad peak that passes through $\nu \approx 10$ GHz over the course of the observations. The peak passes through 10 GHz at around 30 days for AT 2019pim and AT 2021lfa, and at around 10 days for AT 2023lcr.

4. Fitting Framework

4.1. Settings

We use afterglowpy (version 0.7.3; G. Ryan et al. 2020) and MCMC methods in emcee (version 3.1.4; D. Foreman-Mackey et al. 2013) to fit the radio, optical, and X-ray observations of AT 2023lcr with a set of physical parameters that describe the jet and circumburst medium. To put AT 2023lcr's modeling into context, we also perform a consistent analysis on three similarly discovered events, shown in Table 1: AT 2020blt, AT 2021any, and AT 2021lfa. For AT 2019pim and AT 2023sva, see D. A. Perley et al. (2025) and G. P. Srinivasaragavan et al. (2025), which explored similarly broad ranges of scenarios. By contrast, previous works modeling AT 2020blt (N. Sarin et al. 2022), AT 2021any (R. Gupta et al. 2022; F. Xu et al. 2023), and AT 2021lfa (X.-M. Ye et al. 2024) explored more fixed setups.

Table 3
Table of Priors for `afterglowpy`

Parameter	Unit	Description	Prior (Uniform)
t_0	[MJD]	estimated burst time	...
θ_v	[rad]	viewing angle	[0, 1.57]
$\log_{10}(E_{K,iso}/\mathrm{erg})$		isotropic-equivalent kinetic energy of blast wave along jet axis	[45, 57]
θ_c	[rad]	half-opening angle of jet core	[0.02, 0.78]
θ_w	[rad]	wing-truncation angle of a structured jet	$[1, 7] \times \theta_c$
$\log_{10}(n_0/\mathrm{cm}^{-3})$		number density of protons in circumburst medium	[−10, 10]
p		power-law index of relativistic electron energy distribution	[2, 3]
b		power-law index of jet angular energy distribution	[0, 10]
$\log_{10}\epsilon_e$		fraction of thermal energy in relativistic electrons	[−5, 0]
$\log_{10}\epsilon_B$		fraction of thermal energy in magnetic field	[−5, 0]
ξ_N		fraction of accelerated electrons	[0, 1]
$\log_{10}\Gamma_0$		initial Lorentz factor of jet	[0, 3]

Note. Our choice of priors is uniform and broad to minimize bias. θ_w is ignored by the top hat model, and b is only used by the power-law model. For each afterglow, the prior on t_0 spans from its last nondetection to its first detection. We are aware that priors for ϵ_e and ϵ_B allow for $\epsilon_e + \epsilon_B > 1$, but none of the fit results are unphysical.

All data used in this work for AT 2020blt and AT 2021any can be found in A. Y. Q. Ho et al. (2020, 2022). To model AT 2021lfa, we used all observations from A. Y. Q. Ho et al. (2022) and additional observations from V. Lipunov et al. (2022). Optical observations were corrected for Galactic extinction with $E(B - V) = A_V/R_V$, assuming $R_V = 3.1$ (D. J. Schlegel et al. 1998). For all afterglows, we converted X-ray fluxes to a 5 keV flux density assuming a spectral index of $\beta = -1$, where $f_\nu \propto \nu^\beta$.

Our `emcee` settings are as follows. To minimize bias, our priors are broad and uniform (see Table 3). We use the standard `EnsembleSampler` from `emcee`. We perform most runs using 64 walkers and 75,000 iterations, discarding 30,000 iterations as the burn-in. If samples do not appear converged with these settings, we run using 64 walkers and 225,000 iterations, discarding 125,000 as the burn-in. We use a simple Gaussian likelihood for each data point. For AT2020blt, we penalize samples that do not satisfy radio upper limits by finding the log likelihood between the sample-generated radio data point and a zero flux point.

We fit each afterglow to top hat, Gaussian, and power-law jet structures found in `afterglowpy`. The simplest structure is a top hat model, in which energy is constant from the central axis to the edge of the jet:

$$E(\theta) = \begin{cases} E_{K,iso}, & \theta \leqslant \theta_c \\ 0, & \theta > \theta_c \end{cases}, \qquad (2)$$

where $E_{K,iso}$ is the isotropic-equivalent kinetic energy of the outflow along the jet axis and θ_c is the half-opening angle of the jet core. The top hat model offers no extended jet structure, unlike Gaussian or power-law structures, which particularly affects off-axis or even slightly off-axis observations (V. Cunningham et al. 2020; G. Ryan et al. 2020). For a Gaussian structured jet,

$$E(\theta) = \begin{cases} E_{K,iso} \exp\left(-\frac{\theta^2}{2\theta_c^2}\right), & \theta \leqslant \theta_w \\ 0, & \theta > \theta_w \end{cases}, \qquad (3)$$

where the jet extends beyond θ_c to a "wing-truncation angle" θ_w. A power-law structured jet has a similar structure:

$$E(\theta) = E_{K,iso}\left(1 + \frac{\theta^2}{b\theta_c^2}\right)^{-b/2}, \qquad (4)$$

where b is the power-law index at which the jet energy decreases. Because there is structure beyond θ_c in the Gaussian and power-law models, observers are able to view afterglow emission beyond a viewing angle $\theta_v = \theta_c$. In this work, we attempt to describe each afterglow with the simplest possible structure (an on-axis top hat jet). We report the result of other structures only if the afterglow is inconsistent with an on-axis top hat jet (by eye, or has a χ^2/degrees of freedom (DoF) significantly worse than other models).

Along with top hat, Gaussian, and power-law jet structures, we fit each afterglow to various combinations of multi-wavelength observations, since afterglow emission at different wavelengths can reveal different physics. For example, radio observations can capture "reverse shock" emission, which traces a shock propagating back through the outgoing jet shell and toward the central engine, typically crossing this region at the deceleration time (S. Kobayashi & R. Sari 2000; T. Piran 2005; T. Laskar et al. 2016). We fit each model only to optical observations, then only to optical and X-ray observations, then to all radio, optical, and X-ray observations—and report any significant differences in the results.

4.2. Afterglowpy Limitations

`afterglowpy` (version 0.7.3) uses the single-shell approximation (H. van Eerten et al. 2010) to model a blast wave propagating through a homogeneous circumburst medium (G. Ryan et al. 2020). `afterglowpy` is useful for its range of afterglow settings and its implementation of structured jets, but is limited in different ways that could affect our interpretations. For example, if support for inverse Compton cooling (ICC) is enabled, `afterglowpy` overestimates its radiative contribution. Additionally, by default, `afterglowpy` assumes $\Gamma_0 = \infty$, such that there is no initial coasting phase or deceleration break, which might produce unreliable early-time light curves. On the other hand, for a

Table 4
Radiative Energy Upper Limits for AT 2020blt, AT 2021any, AT 2021lfa, and AT 2023lcr

Afterglow	$E_{\gamma,\mathrm{iso}}$ $(10^{52}$ erg$)$	Reference
AT 2020blt	<1.0	A. Y. Q. Ho et al. (2020, 2022)
	<0.1−0.6	N. Sarin et al. (2022)
AT 2021any	<14.3	A. Y. Q. Ho et al. (2022)
AT 2021lfa	<0.12	A. Y. Q. Ho et al. (2022)
AT 2023lcr	<2.1	A. Ridnaia et al. (2023); this work; for $z = 1.0272$
	<4.9	for $z = 1.6$

Note. N. Sarin et al.'s (2022) estimate uses Fermi observations, to which the position of AT 2020blt was not fully visible during the duration between its last nondetection and first detection.

Table 5
Analytical Constraints on the Lorentz Factors for AT 2020blt, AT 2021any, AT 2021lfa, and AT 2023lcr

Afterglow	Rise Time (Γ_0/κ)	Spectrum $(\Gamma_{\mathrm{avg}}^\dagger)$	ISS $(\Gamma_{\mathrm{avg}}^\dagger)$
AT 2020blt	$\gtrsim 19.7$	…	…
AT 2021any	$\gtrsim 81.2$	$\gtrsim 45, \gtrsim 62$	$\lesssim 127, \lesssim 175$
AT 2021lfa	$\gtrsim 10.8, \lesssim 30.0$	$\gtrsim 3, \gtrsim 27$	$\lesssim 6.4, \lesssim 60$
AT 2023lcr	$\gtrsim 37.8$	$\gtrsim 14, \gtrsim 39$	$\lesssim 86, \lesssim 328$

Note. We abbreviate $\kappa = (E_{53}/n_0)^{1/8}$. [†]Left-hand values are average Lorentz factors at the time of first detection. Right-hand values are average Lorentz factors at the beginning of deceleration. We assume a typical rest-frame deceleration time $t_{\mathrm{dec,rest}} \approx t_{\mathrm{rise,rest}} \approx 200$ s, but caution that if AT 2021lfa's rising phase is due to deceleration, then its right-hand values are overestimates.

finite Γ_0, `afterglowpy` disables jet spreading, which might produce unreliable late-time light curves. To work around this, we run MCMC multiple times, with each combination: with and without ICC; and with $\Gamma_0 = \infty$ and $\Gamma_0 \neq \infty$. We report any notable differences in the inferred parameters.

In addition to the above, `afterglowpy` does not support reverse shock physics, which might particularly affect radio observations. Also, `afterglowpy` lacks support for synchrotron self-absorption. In this work, self-absorption affects AT 2021lfa, in which radio observations $\lesssim 21$ days from the estimated burst time may be self-absorbed (A. Y. Q. Ho et al. 2022). There may also be hints of self-absorption in the first few days of AT 2023lcr's SED evolution (see Figure 3 in Section 2). We include all observations in the fit, but caution that the model may be expected to overpredict the radio luminosity at early times (while lacking the reverse shock may result in underpredicting the radio luminosity, particularly at early times).

Finally, `afterglowpy` implements a homogeneous circumburst medium, with no support for a stellar wind medium. Although in principle, a massive star progenitor should have a stellar wind medium, past works have shown that generally, a homogeneous medium fits well to most LGRBs (S. Schulze et al. 2010; J. Hjorth & J. S. Bloom 2011), with some exceptions (A. Panaitescu & P. Kumar 2001).

4.3. Goodness-of-fit Metrics

To quantify the goodness of fit between modeling configurations, we use a reduced χ^2

$$\chi^2 \equiv \frac{1}{\mathrm{DoF}} \sum \frac{(f_{\mathrm{model}} - f_{\mathrm{obs}})^2}{\sigma^2}, \qquad (5)$$

where f_{model} is the model generated light curve, f_{obs} is the observed light curve, σ is the uncertainty (systematic and statistical) in observations, and DoF is the difference between the number of observations and the number of MCMC parameters. In the results that follow, we report the minimum χ^2 over 5000 randomly selected posterior samples. We note that for VLA data, we include a 5% systematic error on the flux densities for the L, S, C, X, and Ku bands (1–18 GHz), and a 15% systematic error for the K and Ka bands (18–40 GHz).

We also use the Widely Available Information Criterion (WAIC; S. Watanabe 2010; V. Cunningham et al. 2020), which can be calculated from MCMC posterior samples. WAIC estimates the "expected log predictive density"

$(\widehat{\mathrm{elpd}})$, which describes how well a model should fit to new data. We do not normalize our WAIC scores, so a more positive $\widehat{\mathrm{elpd}}$ indicates a stronger predictive power. In this paper, we report each $\widehat{\mathrm{elpd}}$ calculated over 5000 randomly selected posterior samples.

4.4. Radiative Efficiencies

To calculate the efficiency of gamma-ray radiation for each event, or "radiative efficiency," we use

$$\eta_\gamma = \frac{E_{\gamma,\mathrm{iso}}}{E_{\mathrm{K,iso}} + E_{\gamma,\mathrm{iso}}}, \qquad (6)$$

where $E_{\mathrm{K,iso}}$ is the isotropic-equivalent kinetic energy of the jet, found from modeling. $E_{\gamma,\mathrm{iso}}$ is the observed isotropic-equivalent energy in gamma-rays, or "radiative energy" from flux or fluence upper limits of gamma-ray facilities. We calculate an $E_{\gamma,\mathrm{iso}}$ upper limit for AT 2023lcr in Section 2.5. Limits for AT 2020blt, AT 2021any, and AT 2021lfa have been calculated in A. Y. Q. Ho et al. (2020), A. Y. Q. Ho et al. (2022), and N. Sarin et al. (2022). We summarize all $E_{\gamma,\mathrm{iso}}$ upper limits in Table 4. We note that the upper limit from N. Sarin et al. (2022) was based on a subthreshold search of Fermi observations, which experienced interruptions between AT 2020blt's last nondetection and first detection.

5. Results and Discussion

5.1. Analytical Constraints on the Lorentz Factors

We follow D. A. Perley et al. (2025) to obtain analytical estimates on the afterglow bulk Lorentz factors, summarizing results in Table 5. Assuming a uniform medium density, we can obtain a limit on the initial Lorentz factor of the jet from the deceleration time using Equation (16) of P. Mészáros (2006),

$$\Gamma_{2.5} = \left(\frac{10\,\mathrm{s}\,(1+z)}{t_{\mathrm{dec}}}\right)^{3/8}\left(\frac{E_{53}}{n_0}\right)^{1/8}, \qquad (7)$$

where z is the redshift, n_0 is the number density of the circumburst medium in cm^{-3}, $E_{53} = E_{\mathrm{K,iso}}/10^{53}$, $\Gamma_{2.5} = \Gamma_0/10^{2.5}$, and t_{dec} is the deceleration time in seconds.[40] Typically, t_{dec} coincides with

---

[40] All times in this work are in the observer frame unless specified otherwise. Rest-frame quantities will be denoted with a subscript, e.g., $t_{\mathrm{rise,rest}}$ for a rest-frame rise time.

the peak of the X-ray afterglow, which occurs on the same timescale as the afterglow rise time. Therefore, we approximate $t_{\rm dec} \approx t_{\rm rise}$, where $t_{\rm rise}$ is the afterglow rise time. Using the difference between the first detection and last nondetection[41] as an upper limit on $t_{\rm rise}$, we obtain the Γ_0 lower limits shown in Table 5, abbreviating $\kappa = (E_{53}/n_0)^{1/8}$. For AT 2021lfa, we also obtain an upper limit on Γ_0, since $t_{\rm rise} > 0.13$ day, which is the time between AT 2021lfa's first MASTER detection and ZTF peak detection.

We can also obtain a lower limit on the average Lorentz factor $\Gamma_{\rm avg}$ from radio spectra using Equation (5) from R. Barniol Duran et al. (2013). We assume a full filling factor and use the time of the last nondetection as a lower limit on the explosion time. Since AT 2020blt lacks multifrequency radio observations, we only perform this calculation on AT 2021any, AT 2021lfa, and AT 2023lcr.

Radio observations of AT 2021any (A. Y. Q. Ho et al. 2022) are unlikely to be impacted by synchrotron self-absorption given their observed spectral indices, so we use observations from its first radio epoch at $\Delta t = 4.91\,$d to estimate $\Gamma_{\rm avg,4.91d} \gtrsim 3.0$ at 4.91 days from its last nondetection. On the other hand, the radio spectra of AT 2021lfa (A. Y. Q. Ho et al. 2022) and AT 2023lcr show possible self-absorption until $\Delta t \approx 20$ days and $\Delta t \approx 6$ days, respectively. Using observations from these epochs, we obtain $\Gamma_{\rm avg,22.69d} \gtrsim 1.1$ for AT 2021lfa and $\Gamma_{\rm avg,6.3d} \gtrsim 2.6$ for AT 2023lcr. Assuming that their light-curve breaks are caused by jet expansion, we can follow T. J. Galama et al. (2003) to extrapolate these estimates to the times of their first detections, obtaining the results in Table 5. We extrapolate AT 2021any and AT 2023lcr using $\Gamma \propto t^{-1/2}$, which holds for post–jet break expansion. AT 2021lfa exhibits no jet break, so for it we use the pre–jet break case $\Gamma \propto t^{-3/8}$.

As discussed in D. A. Perley et al. (2025), $\Gamma_{\rm avg,first}$ is different from Γ_0, which can still be large if $t_{\rm dec}$ is small. To alleviate this uncertainty, we also extrapolate $\Gamma_{\rm avg}$ to $t_{\rm dec}$ to obtain a closer estimate of Γ_0, assuming that Γ is constant from explosion to the start of deceleration. If we take a typical rest-frame LGRB deceleration time $t_{\rm dec,rest} \approx t_{\rm rise,rest} \approx 200\,$s (G. Ghirlanda et al. 2018), we obtain the larger values for $\Gamma_{\rm avg}$ shown along initial estimates in Table 5. We caution that if AT 2021lfa's rising phase is due to deceleration and not off-axis behavior, then its value is an overestimate.

Finally, we obtain upper limits on Γ from the presence of strong interstellar scintillation (ISS), assuming that is responsible for the observed variability in AT 2021any, AT 2021lfa, and AT 2023lcr (AT 2020blt's radio observations are too limited). If a source exhibits strong ISS (radio fluctuations greater than a factor ~ 2) at a frequency near or less than its critical ISS frequency ν_0 (M. A. Walker 2001; D. A. Perley et al. 2025), then the source's size is at most as large as the Fresnel scale θ_{F0} at its location. Given the source size and estimated explosion time, an upper limit on the Lorentz factor can be calculated.

In Table 6, we list approximate timescales T for strong ISS, critical ISS frequencies ν_0, Fresnel scales θ_{F0} at ν_0, and physical sizes of the Fresnel scale D given the angular diameter distances of the three afterglows. From these values, we obtain $\Gamma_{\rm avg,21d} \lesssim 3.4$ for AT 2021any, $\Gamma_{\rm avg,104d} \lesssim 1.4$ for AT 2021lfa, and $\Gamma_{\rm avg,10d} \lesssim 7.1$ for AT 2023lcr. Extrapolating to the times of

---

Table 6
Approximate Durations T of Strong ISS, Critical Frequencies ISS ν_0, Fresnel Scales θ_{F0}, and Physical Sizes of the Fresnel Scale D of AT 2021any, AT 2021lfa, and AT 2023lcr

Afterglow	T (days)	ν_0 (GHz)	θ_{F0} (μarcsec)	D (10^{16} cm)
AT 2021any	21	15	2	5
AT 2021lfa	104	<8	<5	<13
AT 2023lcr	10	9	3.5	9

Note. Critical ISS frequencies and Fresnel scales are found from M. A. Walker (2001).

Table 7
Final Parameters (68% Uncertainty) for the On-axis, Top Hat, $\Gamma_0 \neq \infty$ Configuration for AT 2023lcr
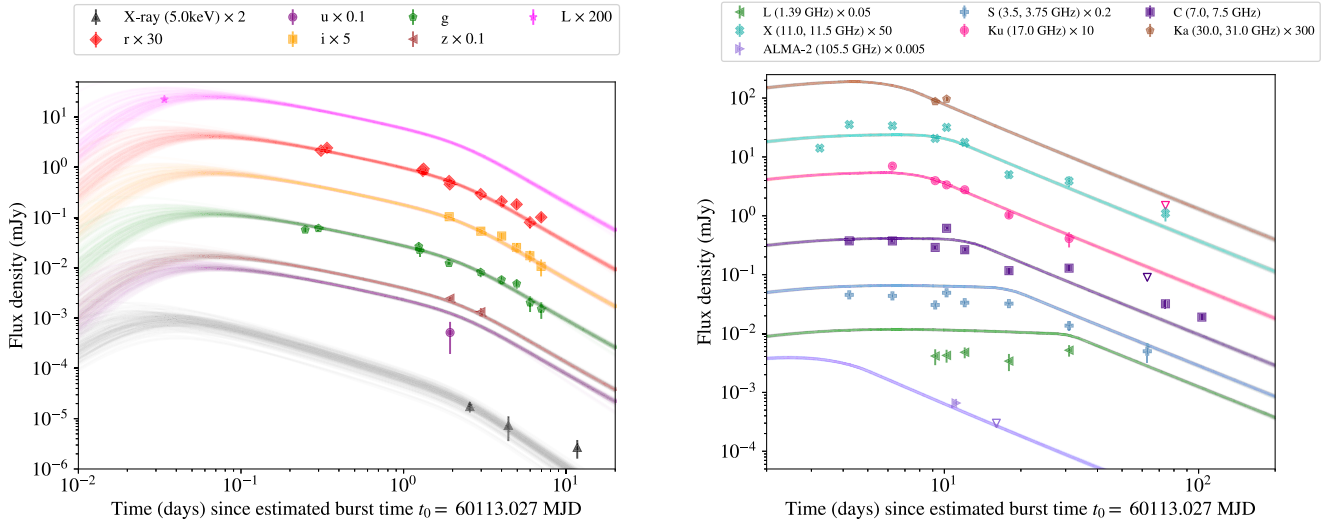
Parameter	Result
t_0 [MJD]	$60113.03^{+0.01}_{-0.02}$
$\theta_{\rm v}$ [rad]	$0.00^{+0.00}_{-0.00}$
$\log_{10}(E_{\rm K,iso}/{\rm erg})$	$53.95^{+0.22}_{-0.17}$
$\theta_{\rm c}$ [rad]	$0.02^{+0.00}_{-0.00}$
$\log_{10}(n_0/{\rm cm}^{-3})$	$-4.37^{+0.53}_{-0.36}$
p	$2.13^{+0.01}_{-0.01}$
$\log_{10}\epsilon_e$	$-1.55^{+0.16}_{-0.22}$
$\log_{10}\epsilon_B$	$-0.63^{+0.32}_{-0.38}$
ξ_N	$0.63^{+0.25}_{-0.24}$
$\log_{10}\Gamma_0$	$2.22^{+0.06}_{-0.09}$
η_γ ($z = 1.0272$)	<1.3%–3.4%
η_γ ($z = 1.6$)	<3.2%–7.5%
χ^2/DoF	14.0
$\widehat{\rm elpd}$	$(-1.7 \pm 0.4) \times 10^2$

Note. We calculate η_γ using the 1σ distribution of $E_{\rm K,iso}$ and the $E_{\gamma,\rm iso}$ limits from Table 4. We present the $\widehat{\rm elpd}$ and minimum χ^2/DoF over 5000 posterior samples; the large χ^2/DoF is due to the overestimation of lower-frequency radio bands (L, S). We ran with 64 walkers and 75,000 iterations; we discarded 25,000.

---

their first detections and deceleration times, we obtain the upper limits found in Table 5.

5.2. AT2023lcr

We present the results of an on-axis top hat jet with a finite Γ_0 in Table 7 and Figure 5, with a corner plot in Figure 11 of Appendix C. The model is able to reproduce key features of all observations, particularly the early-time optical L-band detection and the achromatic break ~ 2 days after the estimated burst time. However, the model somewhat overestimates radio observations in the radio L band (1.39 GHz) and S band (3.75 GHz), which may be due to the susceptibility of low-frequency emission to synchrotron self-absorption, which afterglowpy does not model. The model also slightly overestimates the u-band detection, which may be due to host-galaxy extinction. Fitting configurations with different afterglowpy settings obtained similar results; see Table 17 in Appendix D for results of selected configurations. Optical-only and optical-X-ray-only fits yielded on-axis low Lorentz factor ($\Gamma_0 \sim 30$) GRBs with typical efficiencies and much higher densities ($n_0 \sim 10^{-1}$–$10^{-2}\,{\rm cm}^{-3}$), but had softer

---

[41] The latency is 0.740 day for AT 2020blt, 0.015 day for AT 2021any, 1.794 days for AT 2021lfa, and 0.067 day for AT 2023lcr.

Figure 5. On-axis top hat jet with $\Gamma_0 \approx 166$ for AT 2023lcr, fit to X-ray, optical (left panel), and radio observations (right panel). The model is able to reproduce overall trends in all bands, especially the early-time optical L-band detection, the optical light-curve break, and the X-ray observations. However, the model overestimates the radio L-band (1.39 GHz) and S-band (3.5, 3.75 GHz) detections, likely due to `afterglowpy`'s lack of self-absorption modeling. Plotted are light curves generated from 150 randomly selected posterior samples. Radio upper limits are plotted at $3\times$ image rms.

light-curve breaks at $\Delta t \sim 2$ days and tended to severely overestimate radio detections.

Our results suggest that AT 2023lcr is consistent with an on-axis classical GRB, with a highly collimated jet ($\theta_c \approx 0.02$ rad, or equivalently, $1°.15$) and a low-density circumburst environment ($n_0 \sim 10^{-4}$ cm^{-3}). Calculations on large catalogs of GRBs find most GRBs to have opening angles $\sim 5°$, with few GRBs populating the $\sim 1°$ opening angle regime (A. Goldstein et al. 2016; G. Ghirlanda et al. 2005). While there are GRBs that have circumburst densities as low as 10^{-5} cm^{-3} (see GRB 090423; N. R. Tanvir et al. 2009; R. Salvaterra et al. 2009; T. Laskar et al. 2013), most have circumburst densities within $n_0 = 10^{-1}$–10^2 cm^{-3} (T. Laskar et al. 2013). If AT 2023lcr can be described by a homogeneous medium, then our modeling places AT 2023lcr in a small opening angle, lower-density regime. From the median values in Table 7, we obtain a beaming-corrected value of the blast wave energy $E_K \approx 2.2 \times 10^{50}$ erg, which falls within typical LGRB values of E_K (T. Laskar et al. 2013). We also note that our posterior $\Gamma_0 \approx 166$ is consistent with analytical estimates from Section 5.1.

AT 2023lcr is consistent with an on-axis GRB afterglow, yet KONUS-Wind found no GRB detection while observing the entire night sky during the time between the last GOTO nondetection and first GOTO detection. Therefore, AT 2023lcr had an isotropic radiative energy below 2.1×10^{52} erg and a possible radiative efficiency $\eta_\gamma < 2.3\%$, which is consistent with typical LGRB efficiencies (J. L. Racusin et al. 2011).

5.3. AT2020blt

We present the results of a top hat jet with $\Gamma_0 = \infty$ in Table 8 and Figure 6, with a corner plot in Figure 12 of Appendix C. The model is consistent with optical observations, but underpredicts the X-ray detection by 1.5 orders of magnitude. Other `afterglowpy` configurations produced a similar results, but models with a finite Γ_0 were inconsistent with the ~ 25 days radio nondetection by a factor of 3. We also note that the top hat model we present has the smallest χ^2 and highest predictive power ($\widehat{\mathrm{elpd}}$) of all models attempted for

Table 8
Final Parameters (68% Uncertainty) for the Top Hat, $\Gamma_0 = \infty$ Configuration for AT 2020blt

Parameter	This Work	S22
t_0 [MJD]	$58875.61^{+0.10}_{-0.05}$	$58875.13^{+0.58}_{-1.06}$
θ_v [rad]	$0.08^{+0.08}_{-0.08}$	$0.06^{+0.05}_{-0.04}$
$\log_{10}(E_{K,\mathrm{iso}}/\mathrm{erg})$	$53.00^{+0.67}_{-0.56}$	$53.61^{+0.25}_{-0.35}$
θ_c [rad]	$0.09^{+0.06}_{-0.04}$	$0.14^{+0.04}_{-0.04}$
θ_w	…	$0.42^{+0.16}_{-0.02}$
$\log_{10}(n_0/\mathrm{cm}^{-3})$	$2.05^{+1.15}_{-1.76}$	$1.90^{+1.30}_{-1.72}$
p	$2.83^{+0.13}_{-0.23}$	$2.78^{+0.14}_{-0.20}$
b	…	$5.14^{+2.89}_{-2.76}$
$\log_{10}\epsilon_e$	$-0.63^{+0.41}_{-0.62}$	$-1.10^{+0.34}_{-0.31}$
$\log_{10}\epsilon_B$	$-3.56^{+1.38}_{-0.86}$	$-1.64^{+0.73}_{-0.83}$
ξ_N	$0.46^{+0.35}_{-0.31}$	$0.67^{+0.73}_{-0.83}$
$\log_{10}\Gamma_0$	∞^{a}	$2.70^{+0.21}_{-0.43}$
η_γ	$<2.1\%$–26.6%	$<0.1\%$–3.2%
η_γ (Fermi)	$<0.2\%$–17.9%	$<0.1\%$–3.2%
χ^2/DoF	3.1	…
$\widehat{\mathrm{elpd}}$	$(1.0 \pm 0.1) \times 10^2$	…

Note. We calculate η_γ using the 1σ distribution of $E_{K,\mathrm{iso}}$ and $E_{\gamma,\mathrm{iso}}$ limits from Table 4. We present the $\widehat{\mathrm{elpd}}$ and minimum χ^2/DoF over 5000 posterior samples. We also include the power-law fitting results from N. Sarin et al. (2022). We ran with 64 walkers and 225,000 iterations; we discarded 125,000.
[a] Not from MCMC.

AT 2020blt. See Table 18 in Appendix D for results of selected configurations. We note that modeling AT 2020blt without radio observations showed no significant improvement in the X-ray discrepancy. Optical-only and optical-X-ray-only configurations generally yielded on-axis classical GRBs, some with potentially very low efficiencies ($\eta_\gamma \lesssim 0.1\%$–$1.4\%$; using S22's $E_{\gamma,\mathrm{iso}}$ estimate in Table 4).

From Table 8, we obtain $\theta_c \sim 5°$ and a beaming-corrected $E_K \sim 4 \times 10^{50}$ erg, physical parameters typical of GRBs. However, we acknowledge that all parameters have broad uncertainties due to AT 2020blt's sparse observations. The modeled circumburst density is somewhat high, with
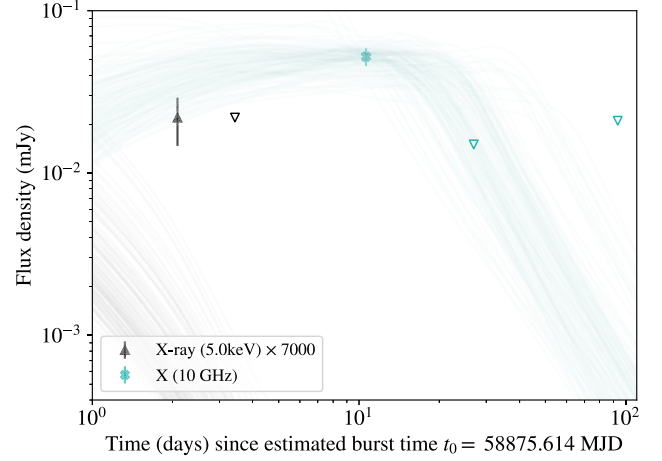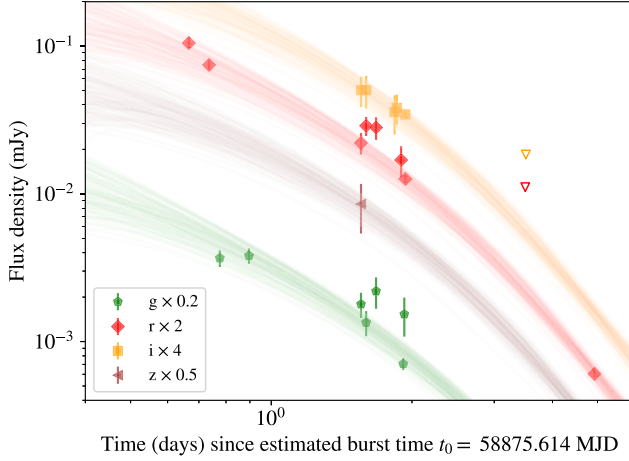
Figure 6. On-axis top hat jet with $\Gamma = \infty$ for AT 2020blt, fit to optical (left panel), X-ray, and radio observations (right panel). Plotted are light curves generated from 150 randomly selected posterior samples. The model is consistent with optical and radio observations, but underestimates the X-ray detection by ~ 1.5 orders of magnitude, possibly due to unmodeled central engine energy injection. Radio upper limits are plotted at $3\times$ image rms.

$n_0 \sim 112$ cm^{-3}, but we note that LGRBs with densities as high as $n_0 \sim 600$ cm^{-3} (see GRB 050904; J. Cummings et al. 2005; G. Tagliaferri et al. 2005; J. B. Haislip et al. 2006; T. Laskar et al. 2013) have been discovered. We also obtain a radiative efficiency $\eta_\gamma < 2.1\%$–26.6% using the KONUS-Wind $E_{\gamma,\mathrm{iso}}$ limit (see Table 4), which is typical of GRBs, as calculated in J. L. Racusin et al. (2011). If we use the less-conservative Fermi $E_{\gamma,\mathrm{iso}}$ limit, we obtain possibly very low efficiencies $\eta_\gamma < 0.2\%$, lower than 98.5% of LGRB efficiencies reported in J. L. Racusin et al. (2011). Our high-Γ fit is also consistent with the lower limits from Section 5.1.

We also obtain values of θ_v that allow for off-axis solutions. We include a comparison between off- and on-axis fits in Figure 7 and Table 9. As expected, the off-axis solution places the peak of the light curve at a later time and has a higher blast wave energy than the on-axis fit. Both fits have comparable χ^2 and $\widehat{\mathrm{elpd}}$ values, suggesting that AT 2020blt is consistent with classical on-axis and off-axis GRBs. Ultimately, we lack the early-time data to resolve the viewing angle degeneracy.

To summarize, we find that AT 2020blt is consistent with off-axis and on-axis classical GRBs. This multimodality may be from sparse observations or from `emcee` and `afterglowpy` limitations; in any case, a classical GRB origin cannot be ruled out for AT 2020blt. We also caution that all fits underestimate the X-ray observation by approximately 1.5 orders of magnitude. This X-ray excess could be from ongoing central engine activity (L. Zhao et al. 2020) or an insufficient χ^2 penalty, since AT 2020blt has only a single X-ray observation with a large uncertainty ($f_{5\,\mathrm{keV}} = 3.14 \pm 1.04\ \mu$Jy).

5.3.1. Comparison to S22

S22 use `afterglowpy` and `dynesty` (J. S. Speagle 2020) to model the optical observations of AT 2020blt with top hat, power law, and cocooned jet structures, and find that AT 2020blt is best explained by an on-axis power-law jet with physical parameters typical of LGRBs, consistent with this work. Using the upper limit for $E_{\gamma,\mathrm{iso}}$ from a subthreshold search on Fermi (see Table 4), which experienced interruptions between AT 2020blt's last nondetection and first detection, S22 explain AT 2020blt as a low-efficiency burst with $\eta_\gamma < 0.1\%$, smaller than 98.5% of LGRB efficiencies from J. L. Racusin et al. (2011). This work reports more typical efficiencies
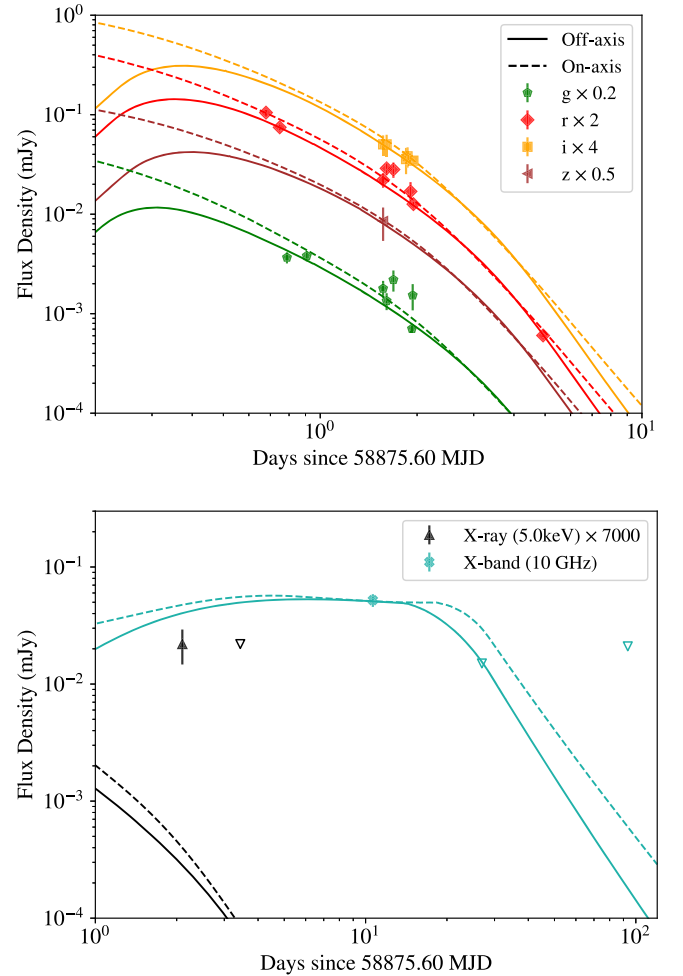
Figure 7. The lowest-likelihood off- and on-axis samples for AT 2020blt, fit to optical (top panel), X-ray, and radio observations (bottom panel). As expected, the off-axis model has a later peak; otherwise, the samples produce similar fits. Radio upper limits are plotted at $3\times$ image rms.

$\eta_\gamma < 2.1\%$–26.6% using the KONUS-Wind upper limit on $E_{\gamma,\mathrm{iso}}$, but does obtain estimates as low as $\eta_\gamma < 0.2\%$ with the Fermi upper limit, consistent with S22. We note that S22 model only the optical observations of AT 2020blt; using the *Fermi*

Table 9
Parameters of Lowest-likelihood Off- and On-axis Solutions

Parameter	Off-axis	On-axis
$\theta_{\rm v}$ [rad]	0.04	0.002
$\theta_{\rm c}$ [rad]	0.02	0.01
t_0 [MJD]	58875.65	58875.55
$\log_{10}(E_{\rm K,iso}/{\rm erg})$	54.0	52.6
$\log_{10}(n_0/{\rm cm}^{-3})$	-1.0	0.09
$\chi^2/{\rm DoF}$	3.1	3.3
$\widehat{\rm elpd}$	104 ± 10	103 ± 9

Note. To calculate the $\widehat{\rm elpd}$, we split the posterior into off-axis and on-axis solution sets and find the $\widehat{\rm elpd}$ over 5000 samples from each set.

estimate, our optical-only configurations also produce efficiencies as low as $\eta_\gamma < 0.1\%$. In any case, both S22 and this work indicate that AT 2020blt is consistent with an on-axis GRB with physical parameters that are fairly typical of the LGRB population.

5.4. AT2021any

We present the results of an on-axis top hat jet with a finite Γ_0 in Table 10 and Figure 8, with a corner plot in Figure 13 of Appendix C. Since the first detection and last nondetection of AT 2021any are only 22 minutes apart, we also fit AT 2021any to an on-axis top hat jet with a fixed burst time $t_0 = 59230.290$ MJD, which we note is an arbitrary choice that lies between the last nondetection and first detection. We present the results of this configuration in Table 10 and Figure 8, with a corner plot in Figure 14 of Appendix C. The free t_0 model places the peak of the light curve before the first ZTF detection, while the fixed t_0 model places it after. This is expected given the earlier burst time found for the free t_0 model in Table 10. There are no other notable differences, and both configurations are able to reproduce all observations. Other afterglowpy configurations are also consistent with observations, except those with ICC enabled, which fail to account for the X-ray observation. See Table 19 in Appendix D for results of selected configurations. Optical-only and optical-X-ray-only fits allowed for potentially off-axis and low-efficiency solutions ($\eta_\gamma \lesssim 0.2\%$–$0.7\%$), all with typical Lorentz factors. However, the potentially off-axis solutions are highly ambiguous given the lack of early-time observations for AT 2021any.

As shown in Table 10, both models also find low-Γ_0 and high-Γ_0 solutions. The free t_0 model finds $\Gamma_0 \approx 204^{+371}_{-115}$, while the fixed t_0 model finds $\Gamma_0 \approx 81^{+17}_{-15}$, indicating that AT 2021any is possibly consistent with both a moderate and ultrarelativistic jet. Ultimately, we lack the higher-cadence early optical data to resolve this degeneracy.

Both models find physical parameters typical of the LGRB population, including an opening angle $\theta_{\rm c} \approx 6°$ and beaming-corrected $E_K \approx 2 \times 10^{51}$ erg. The densities found are somewhat high at $n_0 \sim 300$ cm^{-3}, but as discussed in Section 5.3, this is not physically implausible. The radiative efficiencies found are also typical of LGRBs (J. L. Racusin et al. 2011). Given the uncertainty on Γ_0 in both the afterglowpy fits and the analytical constraints in Section 5.1, we conclude that an on-axis classical GRB origin cannot be ruled out for AT 2021any.

5.4.1. Comparison to G22 and X23

G22 used afterglowpy and emcee to model the optical and X-ray observations of AT 2021any, while X23 use GRB evolution models from Y. F. Huang et al. (2000), Y. F. Huang et al. (2006), J. J. Geng et al. (2013), and F. Xu et al. (2022). Both G22 and X23 set $\xi_N = 1$, and G22 uses a $\Gamma_0 = \infty$afterglowpy configuration. The results from these works are shown in Table 10. G22 found that AT 2021any is consistent with an on-axis classical GRB, while X23 explained AT 2021any as an on-axis GRB with a moderate Lorentz factor $\Gamma_0 = 68$. Differences in physical parameters are likely due to differences in fitting configurations. Notably, both G22 and X23 set $\xi_N = 1$. Past works have shown that different values of ξ_N can significantly change other physical parameters (V. Cunningham et al. 2020), so this is expected; the discrepancies between our results and G22/X24 are consistent with the expected effects of decreasing ξ_N, as discussed in V. Cunningham et al. (2020). However, the physical conclusion is robust: an on-axis classical GRB cannot be ruled out for AT 2021any.

5.5. AT2021lfa

We present the results of an on-axis top hat jet with a finite Γ_0 in Table 11 and Figure 9, with a corner plot in Figure 15 of Appendix C. The model is consistent with optical observations, but underestimates the X-ray detection by $\sim$1 order of magnitude, and overestimates Ku-band (13 GHz) detections at $\Delta t \gtrsim 110$ d by around a factor of 3. We also include in Table 11, Figure 9, and Figure 16 of Appendix C the results of a finite Γ_0 Gaussian jet, which is able to reproduce all observations, but slightly underestimates late-time Ku-band detections.

From Table 11, we obtain a beaming-corrected $E_K \sim 10^{50}$ erg and opening angles $\theta_{\rm c} \approx 4°.6$ and 13°.2, respectively, for the Gaussian and top hat models, typical of the LGRB population (G. Ghirlanda et al. 2018). The Gaussian model also prefers a much denser environment (≈ 4000 cm^{-3}). Both models have very low Lorentz factors, with $\Gamma_0 \approx 11$ for the top hat model and $\Gamma_0 \approx 6$ for the Gaussian model. The Gaussian model also allows for slightly off-axis ($\theta_{\rm v} \sim \theta_{\rm c}$) solutions. The Gaussian model also obtains a possibly low efficiency $\eta_\gamma < 0.5\%$, which is smaller than 98.5% of LGRB efficiencies in J. L. Racusin et al. (2011) but consistent with the $\lesssim$1% efficiencies of internal shocks models (P. Kumar 1999).

All other afterglowpy configurations (see Table 20 in Appendix D for results of selected configurations) produce similar results but still have a strong preference for a very low Lorentz factor jet (typically, $\Gamma_0 \approx 5$–20), consistent with the analytical Γ limits calculated in Section 5.1 and the $\Gamma_0 = 20 \pm 10$ estimate found from V. Lipunov et al. (2022). We note that $\Gamma_0 = \infty$ configurations struggled to reproduce the MASTER observations.

We also fit to a range of data subsets. Optical-only and optical-X-ray-only configurations obtained on- and off-axis solutions, still with low Lorentz factors ($\Gamma_0 \approx 5$–20). We also ran fits that excluded the rising phase, which obtained both classical GRB solutions and on-axis, low-Lorentz-factor solutions. However, we note that the on-axis classical GRB fits underestimated the Ku-band (13.0 GHz) detections at $\Delta t \gtrsim 110$ days by around a factor of 3.
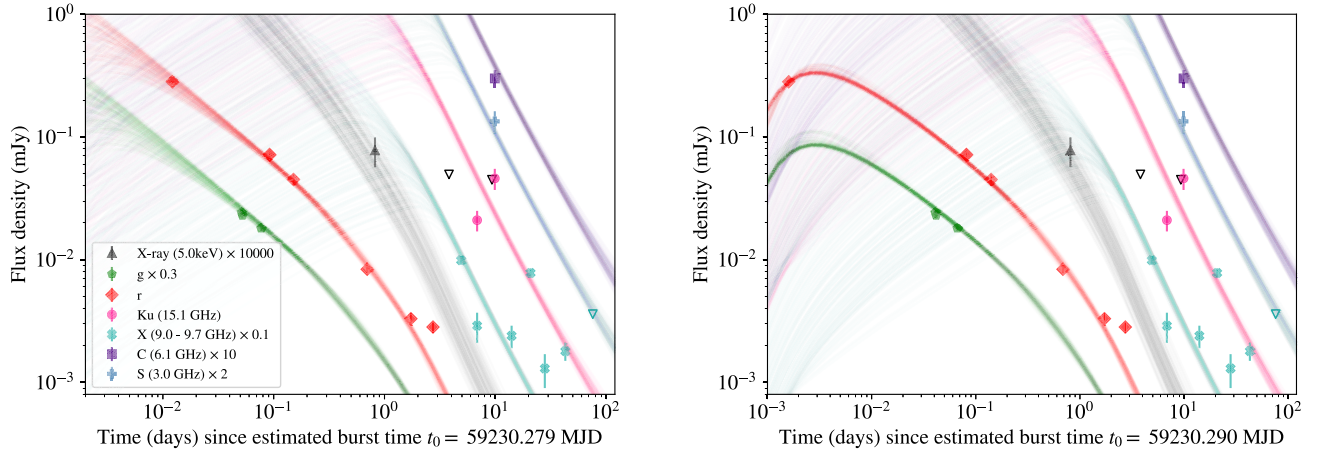
Figure 8. Left panel: on-axis top hat jet with $\Gamma_0 \approx 204$ for AT 2021any where the burst time was allowed to vary. Right: on-axis top hat jet with $\Gamma_0 \approx 81$ and a fixed $t_0 = 59230.290$ MJD. Both models are consistent with optical and X-ray observations, but struggle with radio X-band detections, possibly due to interstellar scintillation. Plotted are light curves generated from 150 randomly selected posterior samples. Radio upper limits are plotted at $3\times$ image rms.

Table 10
Final Parameters (68% Uncertainty) for the On-axis, Top Hat, $\Gamma_0 \neq \infty$, Configurations for AT 2021any

Parameter	Free t_0	Fixed t_0	G22	X24
t_0 [MJD]	$59230.28^{+0.00}_{-0.00}$	59230.29	59230.276[a]	$59230.29^{+0.16}_{-0.12}$
θ_v [rad]	$0.05^{+0.01}_{-0.01}$	$0.05^{+0.01}_{-0.01}$	$0.55^{+0.27}_{-0.27}$	$0.03^{+0.01}_{-0.01}$
$\log_{10}(E_{K,iso}/\mathrm{erg})$	$53.54^{+0.49}_{-0.36}$	$53.60^{+0.34}_{-0.32}$	$52.58^{+0.03}_{-0.03}$	$52.90^{+0.12}_{-0.12}$
θ_c [rad]	$0.10^{+0.03}_{-0.03}$	$0.11^{+0.03}_{-0.02}$	$0.96^{+0.17}_{-0.28}$	$0.08^{+0.01}_{-0.01}$
$\log_{10}(n_0/\mathrm{cm}^{-3})$	$2.41^{+0.56}_{-0.68}$	$2.57^{+0.43}_{-0.43}$	$-0.06^{+0.19}_{-0.17}$	$-0.78^{+0.19}_{-0.19}$
p	$2.01^{+0.01}_{-0.01}$	$2.01^{+0.01}_{-0.00}$	$2.30^{+0.05}_{-0.05}$	$2.39^{+0.02}_{-0.02}$
$\log_{10}\epsilon_e$	$-0.36^{+0.26}_{-0.49}$	$-0.33^{+0.23}_{-0.37}$	-1[b]	$-0.94^{+0.05}_{-0.05}$
$\log_{10}\epsilon_B$	$-4.70^{+0.41}_{-0.22}$	$-4.78^{+0.29}_{-0.16}$	$-2.23^{+0.12}_{-0.13}$	$-2.76^{+0.24}_{-0.24}$
ξ_N	$0.63^{+0.26}_{-0.29}$	$0.68^{+0.22}_{-0.30}$	1[b]	1[b]
$\log_{10}\Gamma_0$	$2.31^{+0.45}_{-0.36}$	$1.91^{+0.08}_{-0.09}$	∞[‡]	$1.92^{+0.06}_{-0.05}$
η_γ	$<11.8\%-48.6\%$	$<14.1\%-42.9\%$	$<77.8-80.1\%$[a]	$<57.7\%-70.3\%$[a]
χ^2/DoF	17.0	13.3	…	…
$\widehat{\mathrm{elpd}}$	$(-1.3 \pm 4.3) \times 10^2$	10.3 ± 31.3	…	…

Note. We calculate η_γ using the 1σ distribution of $E_{K,iso}$ and the $E_{\gamma,iso}$ limits from Table 4. We present the $\widehat{\mathrm{elpd}}$ and minimum χ^2/DoF over 5000 posterior samples. The large values of χ^2/DoF are due to poor fitting in the radio X band (9.0–9.7 GHz). The fixed t_0 model has a more predictive $\widehat{\mathrm{elpd}}$ because it has one less free parameter. We also include top hat configurations from R. Gupta et al. (2022) and F. Xu et al. (2023). We ran with 64 walkers and 75,000 iterations; we discarded 25,000.
[a] G22 and X24 report smaller efficiencies assuming a typical GRB energy fluence threshold $\leqslant 10^{-6}$ erg cm^{-1}; we use a fluence threshold from KONUS-Wind, which is potentially conservative.
[b] Fitting settings.

From our fitting, AT 2021lfa is consistent with on-axis and possibly off-axis low Lorentz factor jets. We explore an off-axis solution in more detail in Section 5.5.2. In any case, the immediate results indicate a strong preference for a jet with $\Gamma_0 = 5$–13, which is remarkably small. The overwhelming majority of classical GRBs report having $\Gamma_0 \gtrsim 100$, with previous calculations on large catalogs of classical GRBs indicating a median $\Gamma_0 = 320$ for a homogeneous circumburst medium (G. Ghirlanda et al. 2018).

Some stellar wind LGRBs with successful prompt emissions have had Lorentz factors as small as $\Gamma_0 \approx 20$ (G. Ghirlanda et al. 2018). Using standard closure relations from Table 1 of B. Zhang & P. Mészáros (2004), we can determine if AT 2021lfa is consistent with having a wind medium. For AT 2021lfa, the optical SED index is $\beta = 0.32 \pm 0.46$ (A. Y. Q. Ho et al. 2022), but the optical temporal index α is uncertain, especially given the large latency (1.79 days)

between the last GOTO nondetection (MJD = 59336.311) and first GOTO detection (MJD = 59338.105). Fitting a single power law to the optical light curve, we find $\alpha \in (1.2, 3.8)$. Considering a typical electron energy power-law index $p \sim 2.3$ (B. Zhang & P. Mészáros 2004), we obtain values for α and β in Table 12, finding that a stellar wind origin for AT 2021lfa cannot be ruled out.

AT 2021lfa could also be the result of a dirty fireball. We estimate the baryon loading of AT 2021lfa with $E_{K,iso} = M\Gamma_0 c^2$ (G. Ghirlanda et al. 2018). From Table 11, we find $M \approx 2.8 \times 10^{-4} M_\odot$ for the top hat model and $M \approx 7.6 \times 10^{-3} M_\odot$ for the Gaussian model, larger than typical LGRB baryon loading values (typically $10^{-6} M_\odot$; G. Ghirlanda et al. 2018) and somewhat larger than the expected baryon loading content required to efficiently produce gamma-rays ($\lesssim 10^{-4} M_\odot$; T. Piran 2005), indicating that AT 2021lfa could be a dirty fireball with strong baryon loading
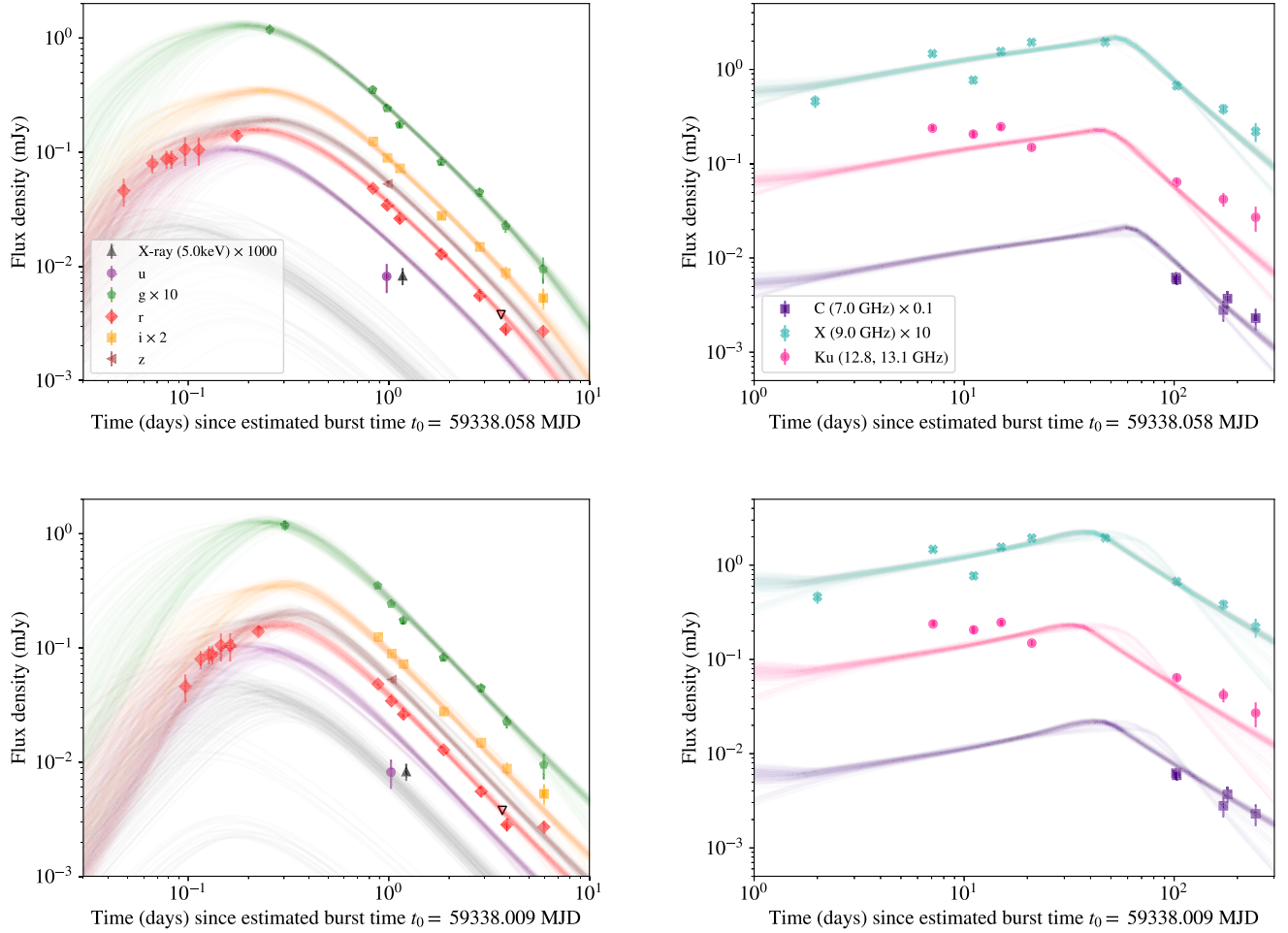
Figure 9. Top panels: on-axis top hat jet with $\Gamma_0 \approx 11.5$ for AT 2021lfa, fit to X-ray, optical (left panel), and radio observations (right panel). The model is consistent with optical and radio observations, but underestimates the X-ray detection by an order of magnitude. Bottom panels: on-axis Gaussian jet with $\Gamma_0 \approx 6.0$ for AT 2021lfa, which is consistent with all observations. Plotted are light curves generated from 150 randomly selected posterior samples.

Table 11
Final Parameters (68% Uncertainty) for the On-axis, Finite Γ_0 Jets for AT 2021lfa

Parameter	Top Hat	Gaussian	Y24
t_0 [MJD]	$59338.06^{+0.01}_{-0.02}$	$59338.01^{+0.03}_{-0.02}$	$59337.92^{+0.08}_{-0.04}$
θ_v [rad]	$0.11^{+0.01}_{-0.01}$	$0.06^{+0.04}_{-0.05}$	$0.53^{+0.18}_{-0.19}$
$\log_{10}(E_{K,iso}/\mathrm{erg})$	$51.76^{+0.46}_{-0.23}$	$52.91^{+0.45}_{-0.52}$	$54.77^{+0.43}_{-0.39}$
θ_c [rad]	$\overset{\circ}{.}$	$0.08^{+0.05}_{-0.03}$	$0.66^{+0.21}_{-0.24}$
θ_w	...	$0.33^{+0.25}_{-0.14}$	...
$\log_{10}(n_0/\mathrm{cm}^{-3})$	$1.11^{+0.42}_{-0.39}$	$3.62^{+0.63}_{-0.88}$	$1.04^{+0.70}_{-0.84}$
p	$2.53^{+0.06}_{-0.05}$	$2.17^{+0.07}_{-0.04}$	$3.09^{+0.03}_{-0.03}$
$\log_{10}\epsilon_e$	$-0.32^{+0.23}_{-0.45}$	$-0.28^{+0.21}_{-0.54}$	$-1.18^{+0.32}_{-0.33}$
$\log_{10}\epsilon_B$	$-1.62^{+0.30}_{-0.39}$	$-3.52^{+0.78}_{-0.61}$	$-4.47^{+0.70}_{-0.38}$
ξ_N	$0.48^{+0.31}_{-0.27}$	$0.11^{+0.06}_{-0.06}$	$0.70^{+0.22}_{-0.27}$
$\log_{10}\Gamma_0$	$1.06^{+0.06}_{-0.05}$	$0.78^{+0.12}_{-0.06}$	$\approx 1.3^{a}$
η_γ	$<6.7\%-26.2\%$	$<0.5\%-4.7\%$	$<0.01\%-0.05\%$
χ^2/DoF	6.0	4.7	...
$\widehat{\mathrm{elpd}}$	77.0 ± 39.4	36.7 ± 43.6	...

Note. We also include results of the top hat configuration from X.-M. Ye et al. (2024). We calculate η_γ with respect to the $E_{\gamma,iso}$ limits from Table 4. We present the $\widehat{\mathrm{elpd}}$ and minimum χ^2/DoF over 5,000 posterior samples. We ran with 64 walkers and 225,000 iterations; we discarded 125,000.
[a] Not from MCMC.

(Y. F. Huang et al. 2002; J. E. Rhoads 2003), and thus low gamma-ray photon production.

5.5.1. Comparison to Y24

Y24 use `afterglowpy` and `emcee` to model all multi-wavelength observations of AT 2021lfa. Similarly to S22, Y24 fits the burst time t_0 independently from other parameters, obtaining $t_{0,Y24} = 59337.92^{+0.08}_{-0.04}$ MJD, consistent within 1σ of our estimated burst times. Otherwise, Y24's physical parameters differ significantly from ours. Notably, Y24 obtained an opening angle $\theta_c \approx 38°$ and a beaming-corrected blast wave energy $E_K \approx 1.3 \times 10^{54}$ erg, which is 4 orders of magnitude greater than our estimate. These values are larger than those of the vast majority of the LGRB population (G. Ghirlanda et al. 2005; T. Laskar et al. 2013; A. Goldstein et al. 2016). The discrepancies between Y24 and this work are likely due to a difference in fitting configurations; Y24 used an `afterglowpy` configuration in which $\Gamma_0 = \infty$ and different priors. Despite configuring $\Gamma_0 = \infty$, Y24 constrained $\Gamma \approx 18$ from Equation (7) using values from their MCMC fit, which is somewhat larger than our results, but still a remarkably low Lorentz factor.

Table 12
Approximate Values of the Optical Temporal Index α and the Optical SED Index β for Various Afterglow Models Using a Typical $p = 2.3$

	α	β
ISM, slow	0.97	0.65
ISM, fast	1.22	1.15
Wind, slow	1.47	0.65
Wind, fast	1.22	1.15
Jet, slow	2.30	0.65

Note. Values were estimated using standard closure relations from B. Zhang & P. Mészáros ([2004](#)). We assume $\nu_m < \nu < \nu_c$ for slow cooling cases and $\nu > \nu_m$ for fast cooling cases.

Table 13
Values around Which the Walkers Were Initialized and Priors for the Forced Off-axis Fit

Parameter	Initial	Prior (Uniform)
t_0 [MJD]	59338.09	[59338.05, 59338.10[a]]
θ_v [rad]	0.16	$[1, 6] \times \theta_c$
$\log_{10}(E_{K,iso} / \mathrm{erg})$	53.14	[45, 57]
θ_c [rad]	0.09	[0.02, 0.78]
θ_w [rad]	0.15	$[1, 7] \times \theta_c$
$\log_{10}(n_0/\mathrm{cm}^{-3})$	-3.73	$[-10, 10]$
p	2.79	[2, 3]
b	5	[0, 10]
$\log_{10} \epsilon_e$	-1.59	$[-5, 0]$
$\log_{10} \epsilon_B$	-1.79	$[-5, 0]$
ξ_N	0.10	[0, 1]
$\log_{10} \Gamma_0$	2.30	[2, 5]

Note. We are aware that priors for ϵ_e and ϵ_B allow for $\epsilon_e + \epsilon_B > 1$, but none of the fit results are unphysical.
[a] In this table, we truncate the time of the first detection (MJD = 59338.1054282), but use all decimal places in our MCMC analysis.

5.5.2. Off-axis Interpretation

AT 2021lfa has a rest-frame rise time $\gtrsim 5600$ s, slower than all upper limits and observed LGRB rise times from G. Ghirlanda et al. ([2018](#)) and R. Hascoët et al. ([2014](#)). Given the relation between $L_{\gamma,iso}$ and rise time, the rise time of AT 2021lfa would imply that any associated LGRB has $L_{\gamma,iso} \lesssim 10^{47}$ erg s^{-1} (G. Ghirlanda et al. [2018](#)), which is consistent with the limit $L_{\gamma,iso} < 2.6 \times 10^{51}$ erg s^{-1} from A. Y. Q. Ho et al. ([2022](#)).

Out of all discovered afterglows without associated detected GRBs, AT 2019pim is the only other event with a confirmed comparably long rest-frame rise time between 1800 and 7200 s. If the rise times of AT 2019pim and AT 2021lfa are due to deceleration viewed on-axis, then it is likely that they are the result of low Lorentz factor jets, as explored in this work and in D. A. Perley et al. ([2025](#)). On the other hand, their long rise times may be due to being viewed off-axis, in which case a high-Γ_0 jet is possible. Indeed, this degeneracy is present in D. A. Perley et al. ([2025](#)), where an on-axis low-Γ_0 jet and a slightly off-axis high-Γ_0 jet are both found as viable solutions for AT 2019pim. We note that if AT 2021lfa's radio fluctuations are due to interstellar scintillation, then AT 2021lfa's scintillation timescale would be ~ 102 days, favoring a low-Γ_0 interpretation (see Section [5](#)). However, fluctuations could be

Table 14
Final Parameters (68% Uncertainty) for the Off-axis, Finite Γ_0 Jets for AT 2021lfa

Parameter	Gaussian	Power Law
t_0 [MJD]	$59338.06^{+0.01}_{-0.00}$	$59338.08^{+0.01}_{-0.01}$
θ_v [rad]	$0.06^{+0.01}_{-0.01}$	$0.13^{+0.01}_{-0.01}$
$\log_{10}(E_{K,iso} / \mathrm{erg})$	$53.14^{+0.85}_{-0.27}$	$52.41^{+0.39}_{-0.23}$
θ_c [rad]	$0.03^{+0.00}_{-0.00}$	$0.10^{+0.01}_{-0.01}$
θ_w [rad]	$0.15^{+0.07}_{-0.06}$	$0.11^{+0.01}_{-0.01}$
$\log_{10}(n_0/\mathrm{cm}^{-3})$	$-2.59^{+0.77}_{-0.39}$	$-0.16^{+0.45}_{-0.43}$
p	$2.96^{+0.02}_{-0.04}$	$2.79^{+0.05}_{-0.05}$
b	...	$4.50^{+3.74}_{-3.38}$
$\log_{10} \epsilon_e$	$-1.37^{+0.27}_{-0.84}$	$-0.75^{+0.22}_{-0.39}$
$\log_{10} \epsilon_B$	$-0.53^{+0.31}_{-0.83}$	$-1.29^{+0.27}_{-0.39}$
ξ_N	$0.44^{+0.37}_{-0.38}$	$0.53^{+0.31}_{-0.31}$
$\log_{10} \Gamma_0$	$2.04^{+0.05}_{-0.03}$	$2.19^{+0.26}_{-0.14}$
η_γ	$< 0.1\% - 1.6\%$	$< 1.9\% - 7.3\%$
χ^2/DoF	5.5	5.5
$\widehat{elpd}$	$(1.1 \pm 0.3) \times 10^2$	$(1.2 \pm 0.3) \times 10^2$

Notes. We calculate η_γ using the 1σ distribution of $E_{K,iso}$ and the $E_{\gamma,iso}$ limits from Table [4](#). We present the $\widehat{elpd}$ and minimum χ^2/DoF over 5000 posterior samples. We ran with 64 walkers and 225,000 iterations; we discarded 125,000.

explained by other effects, such as circumstellar density variations between the early and late-time emission.

Motivated by AT 2021lfa's slow rise time, D. A. Perley et al. ([2025](#)), and off-axis solutions present in the posterior of the former analysis, we explore an off-axis fit for AT 2021lfa. First, we find a plausible off-axis high-Γ_0 solution by manually varying afterglowpy jet parameters, around which we set our priors, shown in Table [13](#). We run Gaussian and power-law configurations, since only structured jets will be able to capture very off-axis ($\theta_v \gtrsim 2 \times \theta_c$) emission. We fit with a finite Γ_0, no ICC, and use all radio, optical, and X-ray observations. We also ran fits with $\Gamma_0 = \infty$, but they were unsuccessful, typically overestimating optical and radio light curves, especially the rising phase MASTER detections. We present the results of our fitting in Table [14](#) and Figure [10](#), with corner plots in Figures [17](#) and [18](#) in Appendix [C](#).

Both models are consistent with optical observations, but the Gaussian model struggles with the finer features of the rising phase r-band detections. The Gaussian fit also includes an optical light-curve break at ~ 0.5 day, which is not present in the power-law fit or the previous on-axis solutions. The models are also consistent with the radio emission at $\Delta t \lesssim 100$ days, similar to the on-axis fits, but underestimate late-time observations at $\gtrsim 110$ days by varying orders of magnitude, at most ~ 0.5. By contrast, the on-axis Gaussian solution (see Figure [5](#)) is generally consistent with late-time radio detections. This discrepancy may favor a wind environment, which would result in shallower light curves. Additionally, the Gaussian and power-law jets underestimate the X-ray detection by ~ 1.5 and ~ 1 orders of magnitude, respectively. In comparison, the on-axis Gaussian solution is able to reproduce to X-ray detection, although the on-axis top hat model struggles by ~ 1 order of magnitude. As previously mentioned, observed X-ray excesses could be due to an ongoing central engine activity (L. Zhao et al. [2020](#)) or, since AT 2021lfa only has a single X-ray detection, an insufficient χ^2 penalty.
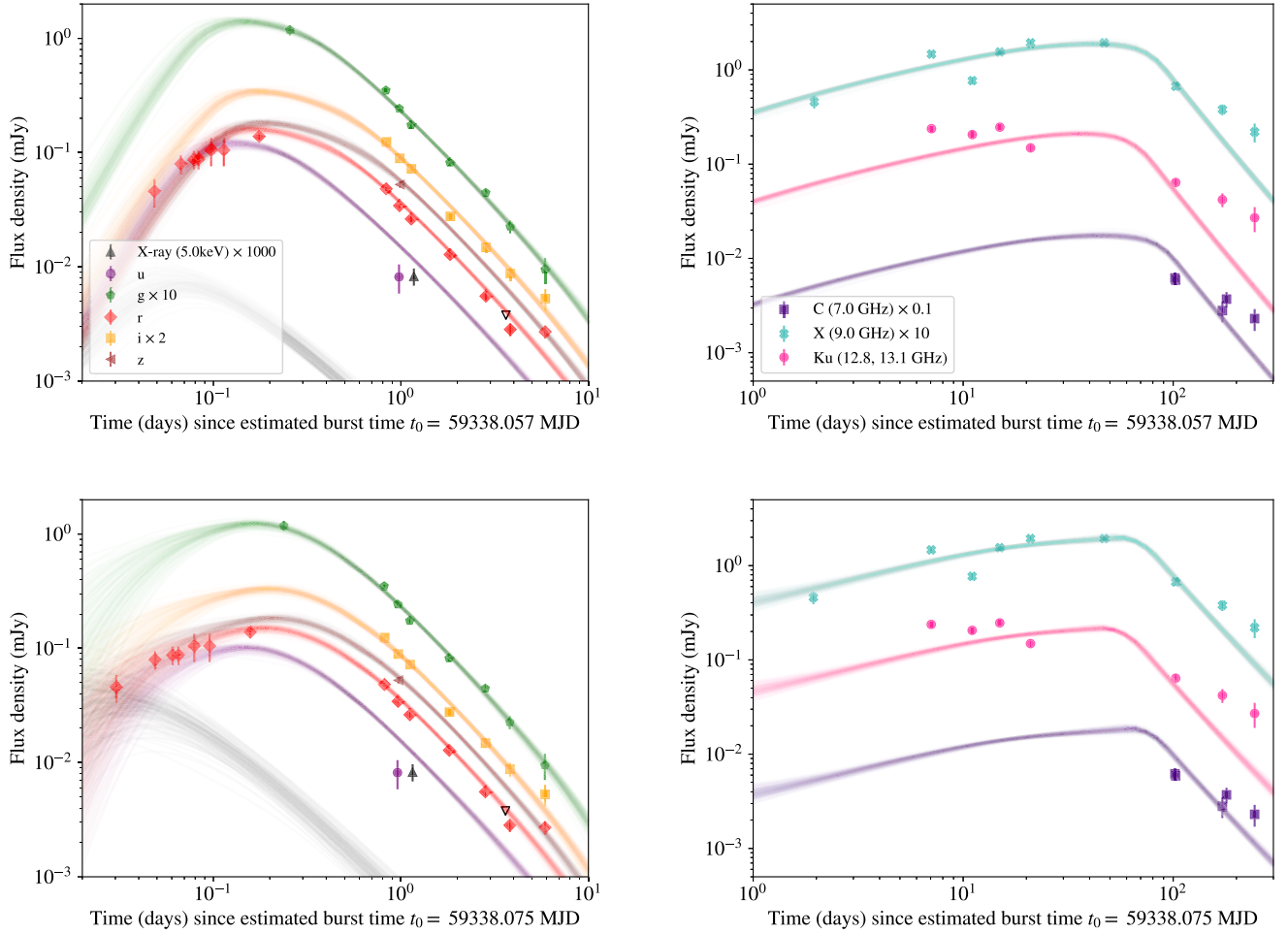
Figure 10. Top panels: off-axis Gaussian jet with $\Gamma_0 \approx 110$ for AT 2021lfa, fit to X-ray, optical (left panel), and radio observations (right panel). The model struggles with the finer features of the rising phase detections. Bottom panels: off-axis power-law jet with $\Gamma_0 \approx 155$ for AT 2021lfa, which is consistent with all optical observations. Both the Gaussian and power-law models overestimate the X-ray detection and late-time radio observations. Plotted are light curves generated from 150 randomly selected posterior samples.

From Table 14, we obtain $\theta_c \approx 1°7$ and $\theta_v \approx 3°4$ for the Gaussian solution, which is very off-axis ($\theta_v \approx 2 \times \theta_c$). For the power-law fit, we obtain $\theta_c \approx 5°7$ and $\theta_v \approx 7°5$, which is less off-axis ($\theta_v \approx 1.3 \times \theta_c$). The Gaussian model obtains a beaming-corrected $E_K \sim 6 \times 10^{49}$ erg while the power-law model obtains a somewhat greater $E_K \sim 10^{50}$ erg, both within typical ranges of LGRB kinetic energies (S.-X. Yi et al. 2017; G. Ghirlanda et al. 2018). Both models obtain typical Lorentz factors, the Gaussian jet with $\Gamma_0 \approx 110$, and a power-law jet with $\Gamma_0 \approx 155$. Lastly, the Gaussian model obtains a possibly low efficiency $\eta_\gamma < 0.1\%$, smaller than 98.5% of bursts in J. L. Racusin et al. (2011).

Generally, the off-axis solutions obtain comparable beaming-corrected kinetic energies ($\sim 10^{50}$ erg), smaller opening angles, and smaller densities to the on-axis fits in Table 11. The off-axis solutions also obtain comparable χ^2/DoFs, but more predictive $\widehat{elpd}$ scores.

Overall, we find that an off-axis high-Γ_0 origin for AT 2021lfa cannot be ruled out. The models' underestimates of late-time radio emission may be due to afterglowpy's lack of jet spreading for the finite Γ_0 setting, and the observed X-ray excesses may be due an insufficient χ^2 penalty on the single X-ray detection or from ongoing central engine activity (L. Zhao et al. 2020).

6. Conclusion

In this work, we presented the identification and multi-wavelength observations of AT 2023lcr, a red, cosmological fast optical transient detected without a GRB trigger. With AT 2023lcr, there are now 10 total afterglows discovered without associated detected GRBs, and six such events with a measured redshift. Using afterglowpy and emcee, we modeled the multiwavelength emission of AT 2023lcr and three similarly discovered afterglows, AT 2020blt, AT 2021any, and AT 2021lfa. We found that a classical on-GRB origin cannot be ruled out for AT 2023lcr, AT 2020blt, and AT 2021any. However, we also found that AT 2020blt and AT 2021any could also be described with nonclassical solutions (off-axis and/or low-Γ_0). The multi-modalities in the solution may be due to a lack of detailed early-time data, but could also arise from emcee/afterglowpy biasing our posteriors to particular locations in parameter space.

Of all afterglows explored in this work, only AT 2021lfa has a convincing nonclassical origin, largely motivated by the slow optical rise time. We found that AT 2021lfa is consistent with both on-axis low Lorentz factor ($\Gamma_0 = 5–13$) and off-axis high Lorentz factor ($\Gamma_0 \approx 100$) jets. The long-lasting fluctuations in AT 2021lfa's radio light curve may favor the low-Γ_0 solution,

implying a smaller radius and therefore slower expansion speed than other events.

We note that without the rise phase of the optical light curve, multiwavelength modeling of AT 2021lfa yields a result consistent with an on-axis classical GRB. Since early-time observations are more sensitive to initial physical conditions, such as the initial Lorentz factor, being able to capture early-time emission is extremely important to constraining an afterglow's origin. The upcoming Argus Array (N. M. Law et al. 2022) promises a high sensitivity, high cadence, and wide field of view, so should be well suited to routinely detect the rising phase.

Our analysis on AT 2021lfa makes it the second afterglow without an associated detected GRB that is consistent with both on-axis low-Γ_0 and off-axis high-Γ_0 solutions, the first being AT 2019pim (D. A. Perley et al. 2025). To resolve the degeneracy, a detection of the prompt emission with wide-field X-ray surveys such as the Einstein Probe (W. Yuan et al. 2022) may be needed. Both dirty fireballs and off-axis GRBs would be expected to be accompanied by an X-ray flash (J. Heise et al. 2001; W. Zhang et al. 2004; T. Sakamoto et al. 2005; A. M. Soderberg et al. 2007), but off-axis afterglow emission should be smoother, while on-axis prompt emission should have shorter-timescale variability. In addition, off-axis GRBs are expected to be accompanied by cocoon emission that peaks in the UV (E. Nakar & T. Piran 2016). Such emission could be detected by the high cadence and sensitivity of the upcoming wide-field survey ULTRASAT (Y. Shvartzvald et al. 2024).

Acknowledgments

Appendix A
Optical Data

We present the optical photometry of AT 2023lcr in Table 15. Magnitudes are in AB and are not corrected for Galactic extinction.

Table 15
Optical Photometry of AT 2023lcr

Start Date (MJD)	Instrument[a]	Filter	Mag
60112.26888	P48	r	>21.61
60112.30249	P48	r	>21.63
60112.31690	P48	i	>20.76
60112.36221	P48	g	>21.67
60112.40275	P48	g	>21.54
60113.27531	P48	g	19.63 ± 0.05
60113.32655	P48	g	19.57 ± 0.05
60113.33749	P48	r	19.29 ± 0.04
60113.36493	P48	r	19.17 ± 0.04
60114.26641	P48	g	20.53 ± 0.15
60114.27940	P48	g	20.73 ± 0.16
60114.32899	P48	r	20.35 ± 0.12
60114.34106	P48	r	20.36 ± 0.10
60114.35403	P48	r	20.24 ± 0.10
60114.40855	P48	g	20.75 ± 0.17
60114.73413	GIT	r	20.67 ± 0.06
60114.77990	GIT	g	21.37 ± 0.15
60114.80649	GIT	i	20.70 ± 0.16
60114.92765	LT	g	21.32 ± 0.08
60114.93103	LT	r	20.88 ± 0.06
60114.93440	LT	i	20.68 ± 0.06
60114.94962	LT	r	21.04 ± 0.06
60114.95300	LT	z	20.47 ± 0.10
60114.95733	LT	u	22.31 ± 0.68
60115.27025	P48	g	>21.65
60115.29196	P48	i	>21.09
60115.31154	P48	r	>21.54
60115.35355	P48	r	20.98 ± 0.19
60115.43086	P48	g	>21.30
60115.70108	GIT	r	21.26 ± 0.08
60116.00182	LT	g	21.77 ± 0.22
60116.00592	LT	r	21.53 ± 0.14
60116.00928	LT	i	21.40 ± 0.16
60116.01265	LT	z	21.14 ± 0.20
60116.71280	GIT	r	21.79 ± 0.08
60117.02526	LT	g	22.14 ± 0.21
60117.03004	LT	r	21.89 ± 0.18
60117.03410	LT	i	21.64 ± 0.19
60117.68238	GIT	g	>21.86
60117.74601	GIT	r	21.92 ± 0.17
60117.97296	LT	i	22.21 ± 0.25
60117.97904	LT	r	22.04 ± 0.20
60117.98509	LT	g	22.34 ± 0.24
60118.70342	GIT	r	22.24 ± 0.10
60118.99971	LT	i	22.62 ± 0.28
60119.00955	LT	r	22.93 ± 0.27
60119.01938	LT	g	23.28 ± 0.38
60119.82540	HCT	r	22.74 ± 0.18
60120.02784	LT	i	23.15 ± 0.40
60120.03768	LT	r	22.68 ± 0.24
60120.04750	LT	g	23.59 ± 0.40

Notes.
[a] P48: Palomar Observatory 48-inch Samuel Oschin Telescope; GIT: GROWTH-India Telescope; LT: Liverpool Telescope.

Appendix B
Radio Data

We present the radio photometry of AT 2023lcr in Table 16. We report upper limits as $3 \times$ the image RMS. We report only the statistical errors, although we include systematic errors in our model fitting, as detailed in Section 4.3.

Table 16
Radio Observations of AT 2023lcr[a]

Epoch	Start MJD	Instrument[b]	ν_{obs} (GHz)	f_ν (μJy)
1	60116.26547	VLA	8.5	109 $\pm$ 9
1	60116.26547	VLA	9.5	140 $\pm$ 9
1	60116.26547	VLA	10.5	164 $\pm$ 9
1	60116.26547	VLA	11.5	282 $\pm$ 11
2	60117.26563	VLA	4.5	267 $\pm$ 11
2	60117.26563	VLA	5.5	256 $\pm$ 11
2	60117.26563	VLA	6.5	257 $\pm$ 10
2	60117.26563	VLA	7.5	375 $\pm$ 10
2	60117.28324	VLA	8.5	561 $\pm$ 11
2	60117.28324	VLA	9.5	625 $\pm$ 10
2	60117.28324	VLA	10.5	666 $\pm$ 11
2	60117.28324	VLA	11.5	710 $\pm$ 12
2	60117.30085	VLA	2.2	48 $\pm$ 21
2	60117.30085	VLA	2.8	35 $\pm$ 19
2	60117.30085	VLA	3.2	151 $\pm$ 16
2	60117.30085	VLA	3.8	227 $\pm$ 16
	60119.14653	SMA	230.0	<600
3	60119.29234	VLA	13.0	631 $\pm$ 11
3	60119.29234	VLA	15.0	672 $\pm$ 10
3	60119.29234	VLA	17.0	699 $\pm$ 13
3	60119.30164	VLA	4.5	298 $\pm$ 14
3	60119.30164	VLA	5.5	382 $\pm$ 12
3	60119.30164	VLA	6.5	356 $\pm$ 11
3	60119.30164	VLA	7.5	374 $\pm$ 11
3	60119.31363	VLA	8.5	516 $\pm$ 12
3	60119.31363	VLA	9.5	582 $\pm$ 12
3	60119.31363	VLA	10.5	621 $\pm$ 12
3	60119.31363	VLA	11.5	677 $\pm$ 13
3	60119.32570	VLA	2.2	108 $\pm$ 21
3	60119.32570	VLA	2.8	112 $\pm$ 18
3	60119.32570	VLA	3.2	192 $\pm$ 16
3	60119.32570	VLA	3.8	218 $\pm$ 15
4	60122.25104	VLA	4.5	144 $\pm$ 14
4	60122.25104	VLA	5.5	200 $\pm$ 14
4	60122.25104	VLA	6.5	242 $\pm$ 12
4	60122.25104	VLA	7.5	290 $\pm$ 12
4	60122.25556	VLA	5.0	151 $\pm$ 14
4	60122.25556	VLA	7.0	235 $\pm$ 13
4	60122.25754	VLA	1.4	83 $\pm$ 25
4	60122.25754	VLA	1.8	52 $\pm$ 18
4	60122.28969	VLA	2.2	102 $\pm$ 21
4	60122.28969	VLA	2.8	100 $\pm$ 18
4	60122.28969	VLA	3.2	151 $\pm$ 16
4	60122.28969	VLA	3.8	153 $\pm$ 16
4	60122.30117	VLA	8.5	352 $\pm$ 13
4	60122.30117	VLA	9.5	396 $\pm$ 8
4	60122.30117	VLA	10.5	394 $\pm$ 13
4	60122.30117	VLA	11.5	412 $\pm$ 14
4	60122.31543	VLA	19.0	410 $\pm$ 14
4	60122.31543	VLA	21.0	432 $\pm$ 21
4	60122.31543	VLA	23.0	372 $\pm$ 36
4	60122.31543	VLA	25.0	376 $\pm$ 19
4	60122.34082	VLA	30.0	292 $\pm$ 21
4	60122.34082	VLA	32.0	340 $\pm$ 25
4	60122.34082	VLA	34.0	370 $\pm$ 24
4	60122.34082	VLA	36.0	316 $\pm$ 26

Table 16
(Continued)

Epoch	Start MJD	Instrument[b]	ν_{obs} (GHz)	f_ν (μJy)
4	60122.36696	VLA	13.0	405 ± 13
4	60122.36696	VLA	15.0	387 ± 13
4	60122.36696	VLA	17.0	395 ± 17
4	60122.37847	VLA	5.0	195 ± 14
4	60122.37847	VLA	7.0	299 ± 12
5	60123.23863	VLA	4.5	322 ± 13
5	60123.23863	VLA	5.5	435 ± 13
5	60123.23863	VLA	6.5	559 ± 12
5	60123.23863	VLA	7.5	613 ± 12
5	60123.24306	VLA	5.0	347 ± 12
5	60123.24306	VLA	7.0	514 ± 12
5	60123.24511	VLA	1.4	85 ± 21
5	60123.24511	VLA	1.8	84 ± 17
5	60123.27727	VLA	2.2	112 ± 17
5	60123.27727	VLA	2.8	123 ± 15
5	60123.27727	VLA	3.2	222 ± 14
5	60123.27727	VLA	3.8	246 ± 12
5	60123.29294	VLA	8.5	690 ± 14
5	60123.29294	VLA	9.5	705 ± 13
5	60123.29294	VLA	10.5	643 ± 10
5	60123.29294	VLA	11.5	635 ± 15
5	60123.31137	VLA	19.0	382 ± 14
5	60123.31137	VLA	21.0	354 ± 19
5	60123.31137	VLA	23.0	378 ± 20
5	60123.31137	VLA	25.0	372 ± 16
5	60123.33328	VLA	31.0	321 ± 19
5	60123.35726	VLA	13.0	456 ± 12
5	60123.35726	VLA	15.0	379 ± 12
5	60123.35726	VLA	17.0	335 ± 15
5	60123.36806	VLA	5.0	372 ± 13
5	60123.36806	VLA	7.0	629 ± 12
	60124.15000	ALMA	90.5	163 ± 29
	60124.15000	ALMA	92.4	166 ± 25
	60124.15000	ALMA	102.5	147 ± 26
	60124.15000	ALMA	105.5	132 ± 23
6	60125.05966	VLA	4.5	191 ± 12
6	60125.05966	VLA	5.5	163 ± 11
6	60125.05966	VLA	6.5	232 ± 11
6	60125.05966	VLA	7.5	265 ± 12
6	60125.06250	VLA	5.0	172 ± 12
6	60125.06250	VLA	7.0	212 ± 12
6	60125.06815	VLA	1.4	96 ± 20
6	60125.06815	VLA	1.8	94 ± 17
6	60125.08433	VLA	2.2	109 ± 18
6	60125.08433	VLA	2.8	153 ± 15
6	60125.08433	VLA	3.2	150 ± 13
6	60125.08433	VLA	3.8	167 ± 13
6	60125.10000	VLA	8.5	324 ± 14
6	60125.10000	VLA	9.5	361 ± 13
6	60125.10000	VLA	10.5	340 ± 13
6	60125.10000	VLA	11.5	353 ± 15
6	60125.11298	VLA	13.0	336 ± 12
6	60125.11298	VLA	15.0	298 ± 11
6	60125.11298	VLA	17.0	277 ± 15
6	60125.12500	VLA	5.0	212 ± 12
6	60125.12500	VLA	7.0	256 ± 12
	60129.04549	ALMA	90.5	139 ± 20
	60129.04549	ALMA	92.4	120 ± 18
	60129.04549	ALMA	102.5	<69
	60129.04549	ALMA	105.5	<60
7	60130.99178	VLA	4.5	148 ± 9
7	60130.99178	VLA	5.5	115 ± 9
7	60130.99178	VLA	6.5	108 ± 12
7	60130.99178	VLA	7.5	117 ± 13

Table 16
(Continued)

Epoch	Start MJD	Instrument[b]	ν_{obs} (GHz)	f_ν (μJy)
7	60130.99306	VLA	5.0	141 ± 15
7	60130.99306	VLA	7.0	89 ± 13
7	60130.99826	VLA	1.4	68 ± 22
7	60130.99826	VLA	1.8	143 ± 19
7	60131.01449	VLA	2.2	158 ± 21
7	60131.01449	VLA	2.8	142 ± 16
7	60131.01449	VLA	3.2	124 ± 14
7	60131.01449	VLA	3.8	161 ± 13
7	60131.03141	VLA	8.5	135 ± 13
7	60131.03141	VLA	9.5	107 ± 12
7	60131.03141	VLA	10.5	92 ± 10
7	60131.03141	VLA	11.5	100 ± 15
7	60131.04550	VLA	20.0	94 ± 15
7	60131.04550	VLA	24.0	92 ± 17
7	60131.06055	VLA	13.0	137 ± 12
7	60131.06055	VLA	15.0	131 ± 11
7	60131.06055	VLA	17.0	103 ± 14
7	60131.07292	VLA	5.0	162 ± 14
7	60131.07292	VLA	7.0	147 ± 12
8	60143.98697	VLA	4.5	113 ± 13
8	60143.98697	VLA	5.5	124 ± 12
8	60143.98697	VLA	6.5	123 ± 13
8	60143.98697	VLA	7.5	129 ± 13
8	60143.98958	VLA	5.0	91 ± 15
8	60143.98958	VLA	7.0	102 ± 13
8	60143.99346	VLA	1.4	104 ± 23
8	60143.99346	VLA	1.8	68 ± 20
8	60144.00969	VLA	2.2	41 ± 20
8	60144.00969	VLA	2.8	80 ± 16
8	60144.00969	VLA	3.2	77 ± 14
8	60144.00969	VLA	3.8	68 ± 13
8	60144.02565	VLA	8.5	110 ± 15
8	60144.02565	VLA	9.5	110 ± 15
8	60144.02565	VLA	10.5	99 ± 15
8	60144.02565	VLA	11.5	78 ± 16
8	60144.03977	VLA	13.0	40 ± 16
8	60144.03977	VLA	15.0	51 ± 10
8	60144.03977	VLA	17.0	41 ± 12
8	60144.05556	VLA	5.0	152 ± 13
8	60144.05556	VLA	7.0	152 ± 12
9	60175.63000	GMRT	1.4	135 ± 26
9	60175.87542	VLA	5.0	32 ± 10
9	60175.87542	VLA	7.0	0 ± 30
9	60175.88190	VLA	3.5	25 ± 9
9	60175.90322	VLA	10.0	0 ± 29
	60177.63000	GMRT	0.6	<90
	60178.63000	GMRT	0.4	<420
10	60187.11613	VLA	5.0	46 ± 6
10	60187.11613	VLA	7.0	32 ± 6
10	60187.13373	VLA	9.0	23 ± 6
10	60187.13373	VLA	11.0	22 ± 6
10	60187.15885	VLA	13.0	35 ± 9
10	60187.15885	VLA	15.0	35 ± 9
10	60187.15885	VLA	17.0	0 ± 50
11	60216.00837	VLA	5.0	23 ± 3
11	60216.00837	VLA	7.0	19 ± 2

Notes.
[a] Epochs of VLA observations are numbered.
[b] VLA: Karl G. Jansky Very Large Array; SMA: Submillimeter Array; ALMA: Atacama Large Millimeter/submillimeter Array; GMRT: Giant Metrewave Radio Telescope.

Appendix C
Corner Plots

We present the corner plots (68% uncertainties) of the models described in Section 5. Figures 11, 12, and 13 present the on-axis top hat models for AT 2023lcr, AT 2020blt, and AT 202any. Figure 14 presents the fixed burst time model of AT 2021any. Figures 15 and 16 present the on-axis models of AT 2021lfa, while Figures 17 and 18 present the off-axis models of AT 2021lfa.
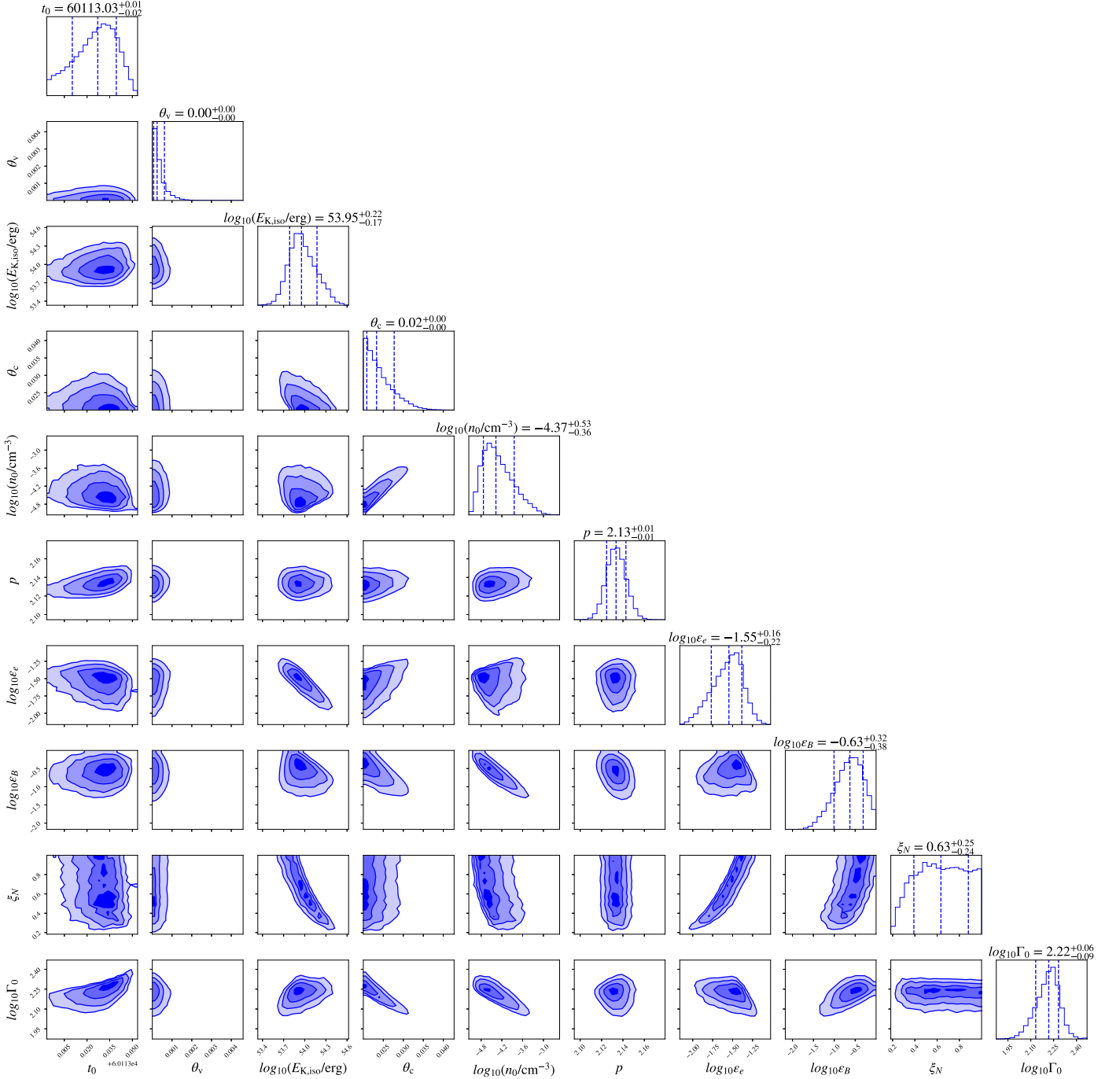
Figure 11. Corner plots (68% uncertainties) of the on-axis, $\Gamma_0 \approx 166$, top hat configuration for AT 2023lcr. We ran with 64 walkers and 75,000 iterations; we discarded 25,000.
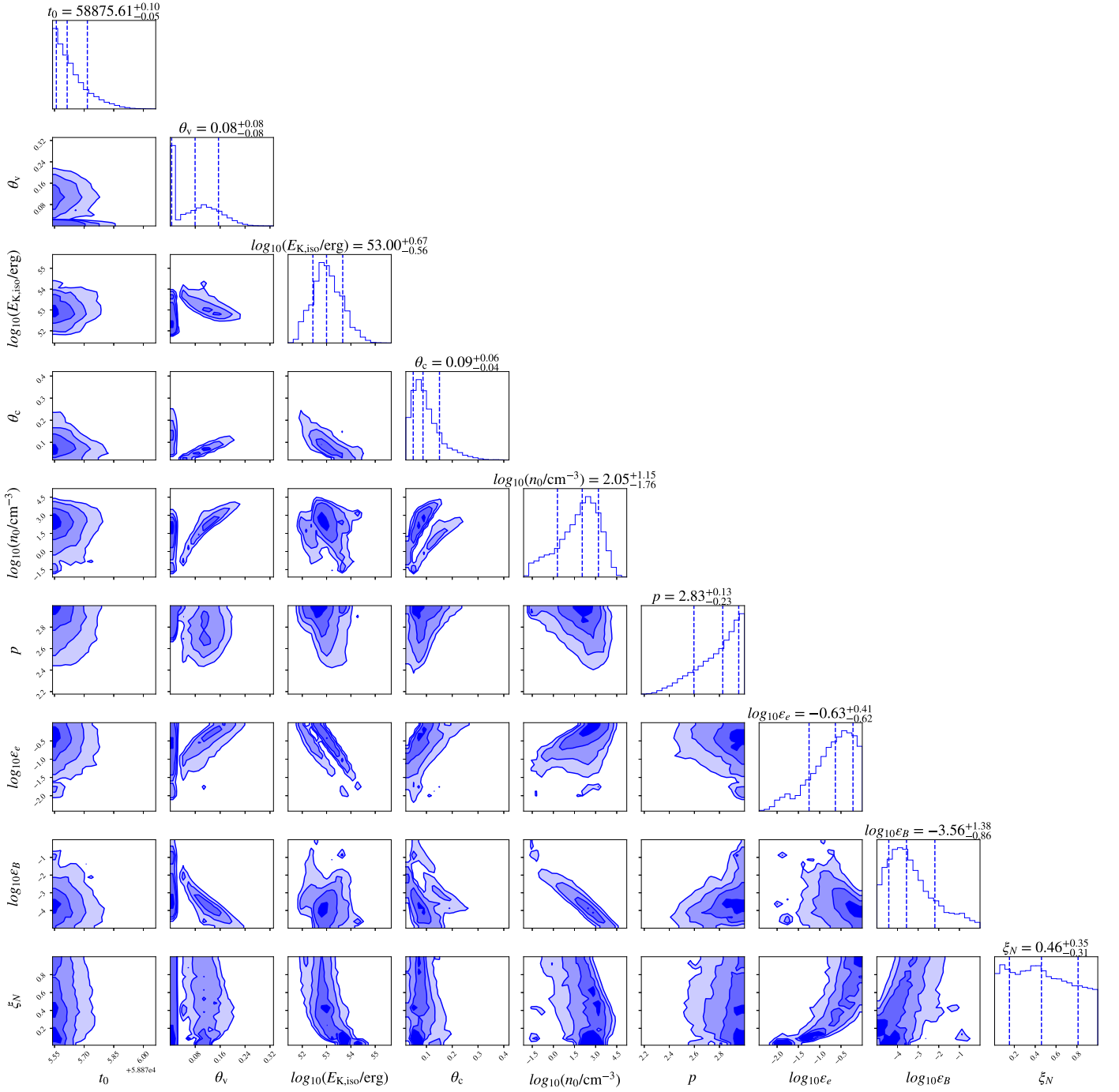
Figure 12. Corner plots (68% uncertainties) of the on-axis, $\Gamma_0 = \infty$, top hat configuration for AT 2020blt. We ran with 64 walkers and 225,000 iterations; we discarded 125,000.
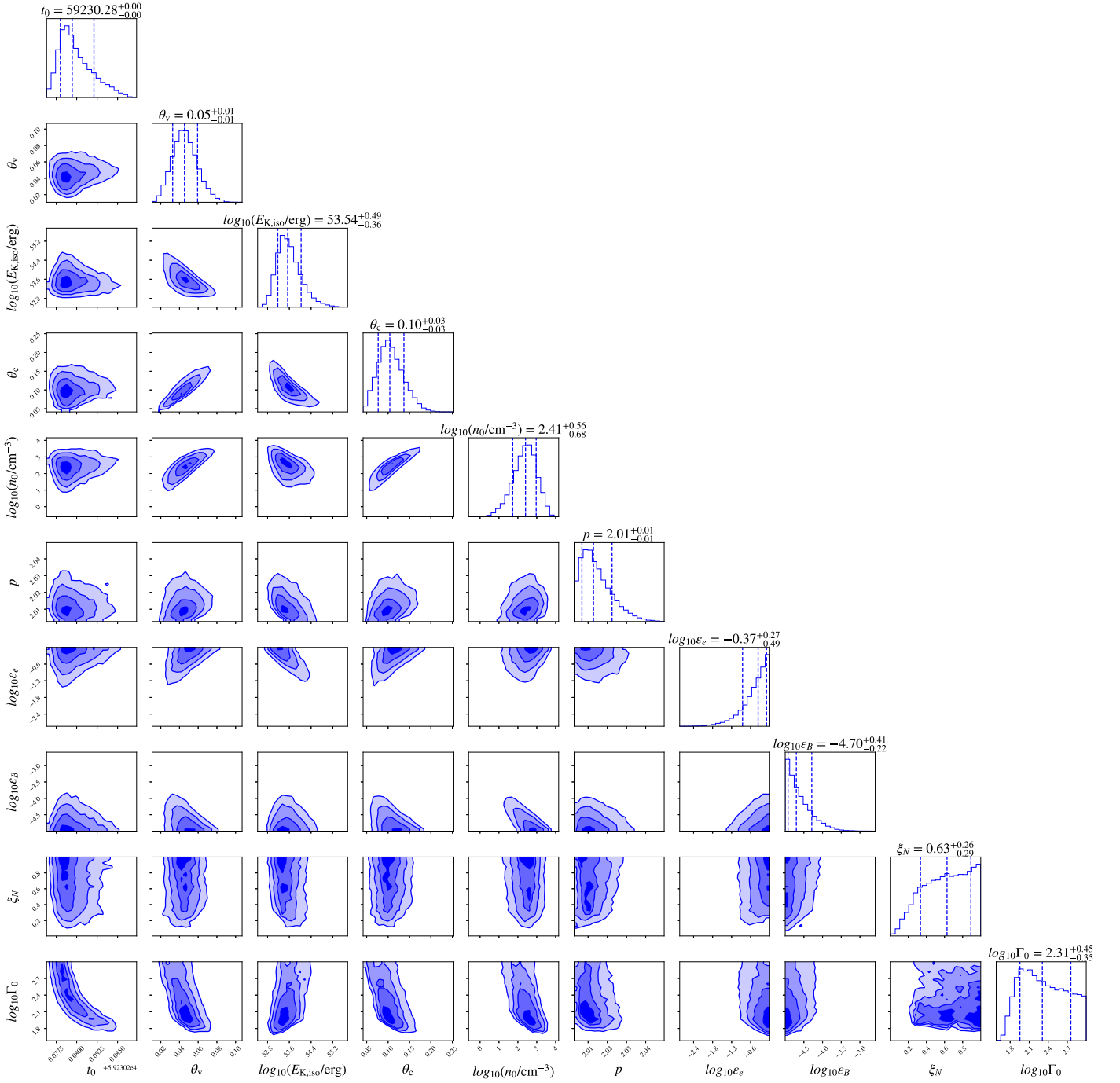
Figure 13. Corner plots (68% uncertainties) of the on-axis, $\Gamma_0 \neq \infty$, top hat configuration for AT 2021any. We ran with 64 walkers and 75,000 iterations; we discarded 25,000.
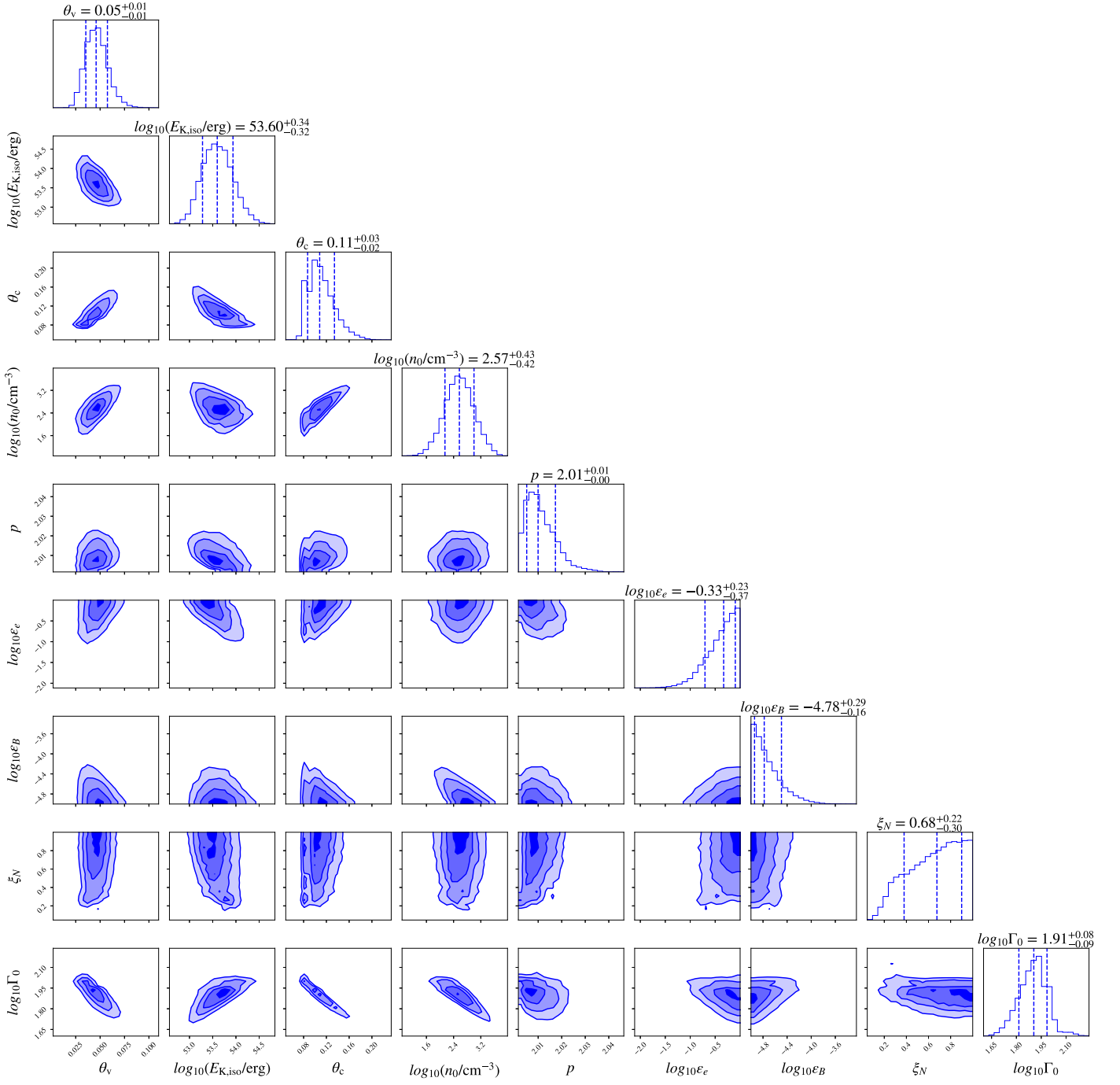
Figure 14. Corner plots (68% uncertainties) of the on-axis, fixed $t_0 = 59230.290$ MJD, $\Gamma_0 \neq \infty$, top hat configuration for AT 2021any. We ran with 64 walkers and 75,000 iterations; we discarded 25,000.
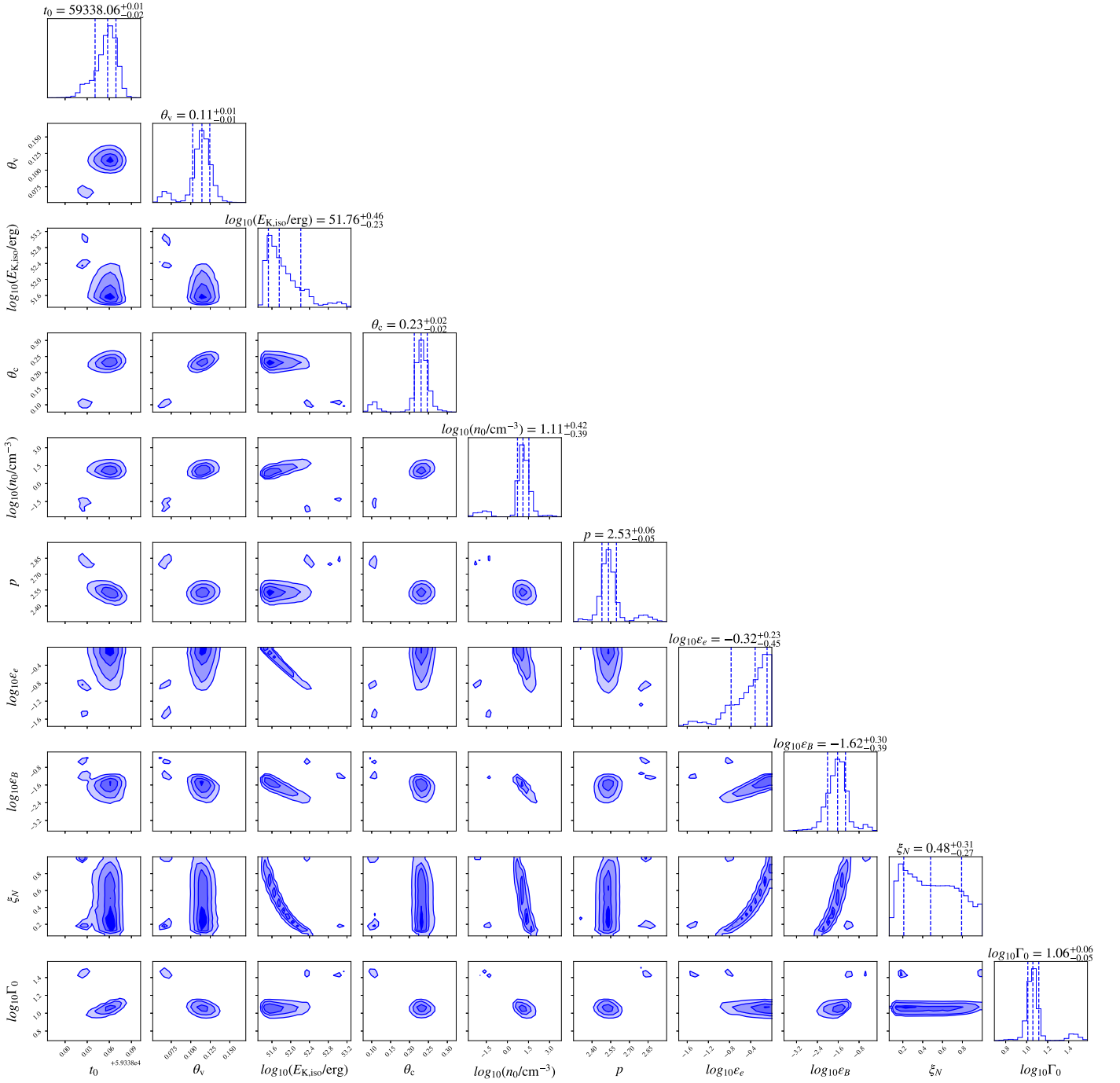
Figure 15. Corner plots (68% uncertainties) of the on-axis, $\Gamma_0 \neq \infty$, top hat configuration for AT 2021lfa. We ran with 64 walkers and 225,000 iterations; we discarded 125,000.
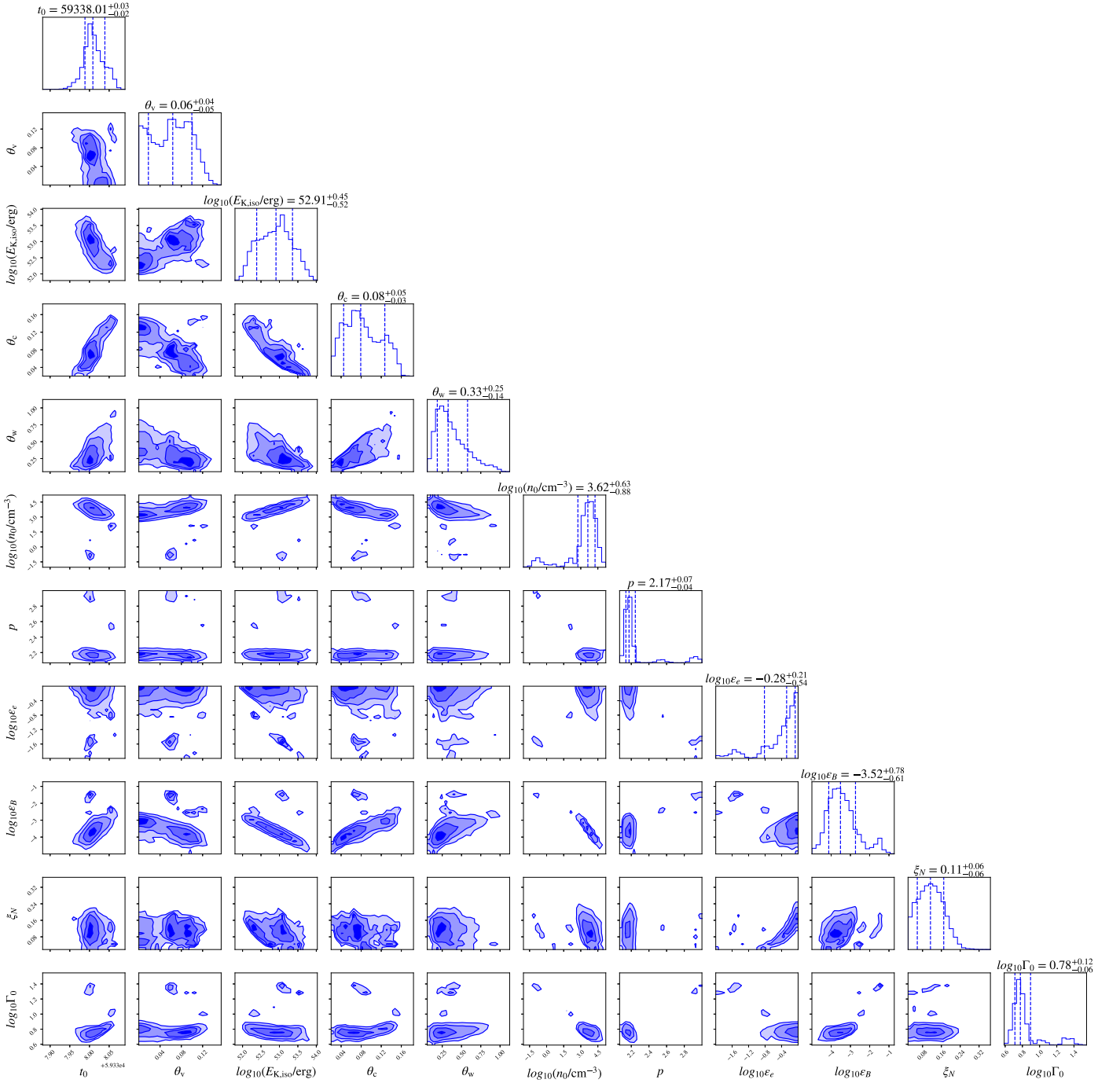
Figure 16. Corner plots (68% uncertainties) of the on-axis, $\Gamma_0 \neq \infty$, Gaussian configuration for AT 2021lfa. We ran with 64 walkers and 225,000 iterations; we discarded 125,000.
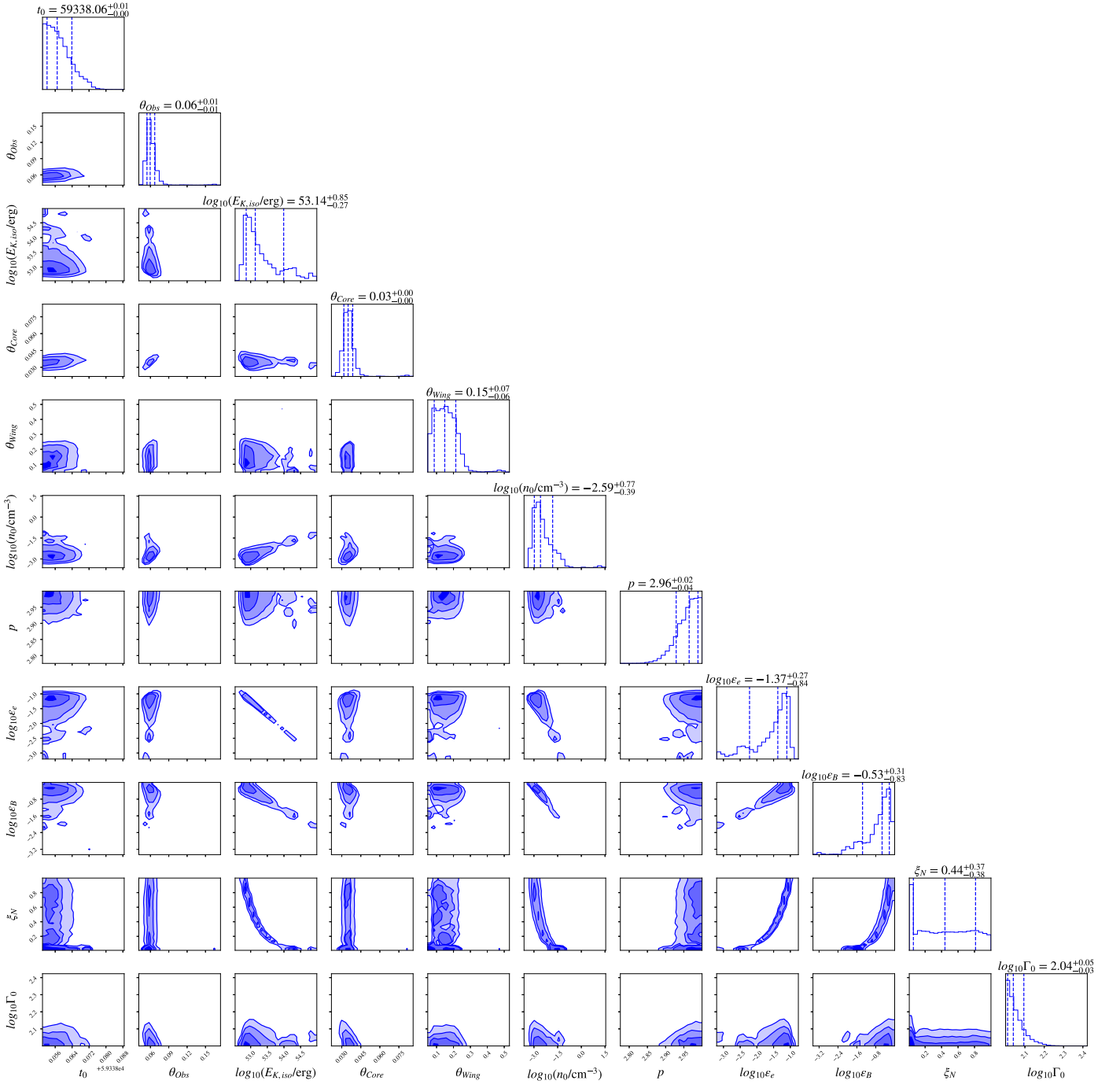
Figure 17. Corner plots (68% uncertainties) of the off-axis, $\Gamma_0 \neq \infty$, Gaussian configuration for AT 2021lfa. We ran with 64 walkers and 225,000 iterations; we discarded 125,000.
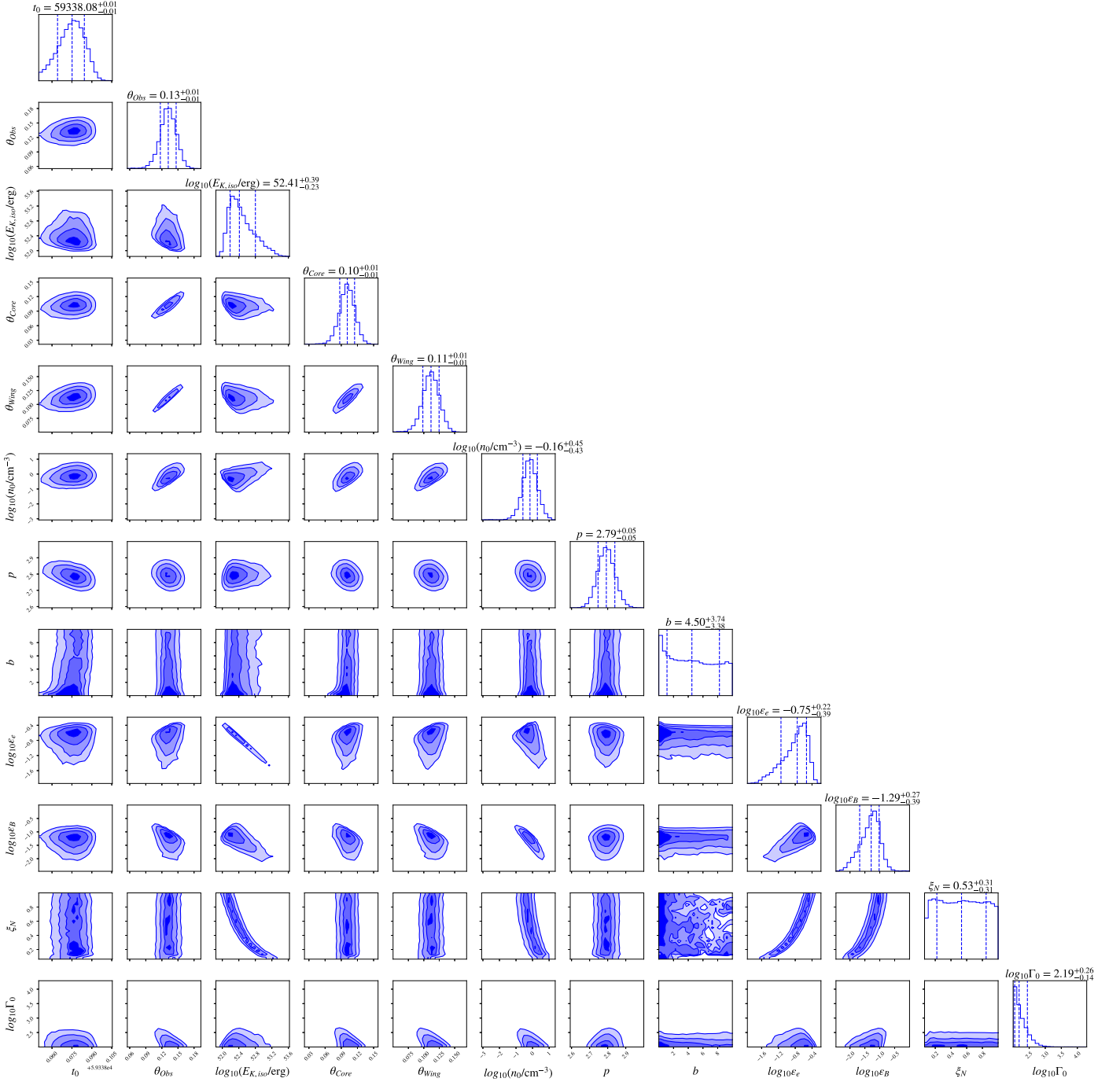
Figure 18. Corner plots (68% uncertainties) of the off-axis, $\Gamma_0 \neq \infty$, power-law configuration for AT 2021lfa. We ran with 64 walkers and 225,000 iterations; we discarded 125,000.

Appendix D
Selected Configurations

For each afterglow, we present the posteriors (68% uncertainties) of other MCMC configurations that were attempted but not presented in Section 5. Table 17 presents AT 2023lcr, Table 18 presents AT 2020blt, Table 19 presents AT 2021any, and Table 20 presents AT 2021lfa.

Table 17
Final Parameters (68% Uncertainty) for Selected Configurations of AT 2023lcr

Parameter	Gaussian	Top Hat (ICC)	Top Hat ($\Gamma_0 = \infty$)
t_0 [MJD]	$60113.03^{+0.01}_{-0.02}$	$60113.02^{+0.01}_{-0.02}$	$60112.99^{+0.00}_{-0.00}$
$\theta_{\rm v}$ [rad	$0.00^{+0.00}_{-0.00}$	$0.00^{+0.00}_{-0.00}$	$0.00^{+0.00}_{-0.00}$
$\log_{10}(E_{\rm K,iso}/\rm erg)$	$53.93^{+0.22}_{-0.17}$	$54.14^{+0.67}_{-0.27}$	$54.51^{+0.25}_{-0.20}$
$\theta_{\rm c}$ [rad]	$0.02^{+0.00}_{-0.00}$	$0.03^{+0.00}_{-0.01}$	$0.02^{+0.00}_{-0.00}$
$\theta_{\rm w}$	$0.02^{+0.00}_{-0.00}$	...	...
$\log_{10}(n_0/\rm cm^{-3})$	$-4.20^{+0.54}_{-0.41}$	$-3.81^{+1.21}_{-0.74}$	$-5.22^{+0.25}_{-0.19}$
p	$2.14^{+0.01}_{-0.01}$	$2.14^{+0.01}_{-0.01}$	$2.09^{+0.01}_{-0.01}$
$\log_{10}\epsilon_e$	$-1.52^{+0.16}_{-0.22}$	$-1.42^{+0.48}_{-0.29}$	$-2.23^{+0.24}_{-0.28}$
$\log_{10}\epsilon_B$	$-0.73^{+0.34}_{-0.40}$	$-1.16^{+0.66}_{-2.89}$	$-0.21^{+0.15}_{-0.26}$
ξ_N	$0.63^{+0.24}_{-0.25}$	$0.60^{+0.27}_{-0.25}$	$0.20^{+0.14}_{-0.09}$
$\log_{10}\Gamma_0$	$2.19^{+0.07}_{-0.08}$	$2.15^{+0.10}_{-0.09}$	∞
η_γ ($z = 1.0272$)	$<1.5\%-3.5\%$	$<0.3\%-2.8\%$	$<0.4\%-1.0\%$
η_γ ($z = 1.6$)	$<3.4\%-7.8\%$	$<0.8\%-6.2\%$	$<0.8\%-2.3\%$
$\chi^2/\rm DoF$	10.8	7.9	14.3
$\widehat{\rm elpd}$	$(-5.7 \pm 7.9) \times 10^2$	31.8 ± 62.3	$(-2.5 \pm 2.2) \times 10^2$

Note. We calculate η_γ using the 1σ distribution of $E_{\rm K,iso}$ and the $E_{\gamma,\rm iso}$ limits from Table 4. We present the $\widehat{\rm elpd}$ and minimum $\chi^2/\rm DoF$ over 5000 posterior samples. We ran with 64 walkers and 75,000 iterations; we discarded 25,000.

Table 18
Final Parameters (68% Uncertainty) for Selected Configurations of AT 2020blt

Parameter	Gaussian[b] ($\Gamma_0 \neq \infty$)	Top Hat[b] (ICC, $\Gamma_0 \neq \infty$)	Top Hat[b] ($\Gamma_0 \neq \infty$)
t_0 [MJD]	$58875.67^{+0.11}_{-0.08}$	$58875.78^{+0.13}_{-0.12}$	$58875.66^{+0.11}_{-0.08}$
$\theta_{\rm v}$ [rad]	$0.09^{+0.04}_{-0.04}$	$0.01^{+0.01}_{-0.00}$	$0.07^{+0.05}_{-0.07}$
$\log_{10}(E_{\rm K,iso}/\rm erg)$	$52.77^{+0.58}_{-0.53}$	$53.56^{+0.84}_{-0.75}$	$52.97^{+0.71}_{-0.88}$
$\theta_{\rm c}$ [rad]	$0.05^{+0.03}_{-0.02}$	$0.08^{+0.01}_{-0.01}$	$0.07^{+0.09}_{-0.03}$
$\theta_{\rm w}$	$0.16^{+0.14}_{-0.08}$	...	...
$\log_{10}(n_0/\rm cm^{-3})$	$1.91^{+1.00}_{-1.02}$	$0.47^{+1.16}_{-0.64}$	$1.85^{+1.10}_{-1.24}$
p	$2.96^{+0.03}_{-0.06}$	$2.95^{+0.04}_{-0.08}$	$2.95^{+0.03}_{-0.06}$
$\log_{10}\epsilon_e$	$-0.47^{+0.28}_{-0.43}$	$-0.94^{+0.55}_{-1.06}$	$-0.58^{+0.33}_{-0.44}$
$\log_{10}\epsilon_B$	$-2.51^{+1.13}_{-1.33}$	$-2.98^{+1.39}_{-1.32}$	$-2.74^{+1.31}_{-1.39}$
ξ_N	$0.49^{+0.32}_{-0.29}$	$0.23^{+0.48}_{-0.21}$	$0.51^{+0.32}_{-0.32}$
$\log_{10}\Gamma_0$	$2.11^{+0.50}_{-0.41}$	$2.49^{+0.35}_{-0.42}$	$2.00^{+0.54}_{-0.50}$
η_γ	$<4.3\%-36.5\%$	$<0.4\%-13.4\%$	$<2.0\%-44.8\%$
η_γ (*Fermi*)	$<0.4\%-5.4\%$	$<0.04\%-1.5\%$	$<0.2\%-7.5\%$
χ^{2}[a]	3.6	3.5	3.4
$\widehat{\rm elpd}$	38.9 ± 38.2	47.1 ± 35.1	5.3 ± 60.5

Note. We calculate η_γ using the 1σ distribution of $E_{\rm K,iso}$ and the $E_{\gamma,\rm iso}$ limits from Table 4. We present the $\widehat{\rm elpd}$ and minimum $\chi^2/\rm DoF$ over 5000 posterior samples. We ran with 64 walkers and 75,000 iterations; we discarded 25,000.
[a] χ^2 does not account for nondetections.
[b] Fails to account for the radio nondetection at ~25 days and struggles or fails with the radio nondetection at ~100 days.

Table 19
Final Parameters (68% Uncertainty) for Selected Configurations of AT 2021any

Parameter	Gaussian	Top Hat (ICC)	Top Hat ($\Gamma_0 = \infty$)
t_0 [MJD]	$59230.28^{+0.00}_{-0.00}$	$59230.29^{+0.00}_{-0.00}$	$59230.28^{+0.00}_{-0.00}$
θ_v [rad]	$0.04^{+0.01}_{-0.01}$	$0.03^{+0.01}_{-0.00}$	$0.04^{+0.03}_{-0.02}$
$\log_{10}(E_{K,iso}/\mathrm{erg})$	$53.31^{+0.42}_{-0.32}$	$53.87^{+0.62}_{-0.53}$	$53.94^{+1.33}_{-0.73}$
θ_c [rad]	$0.09^{+0.02}_{-0.02}$	$0.03^{+0.01}_{-0.01}$	$0.08^{+0.07}_{-0.05}$
θ_w	$0.34^{+0.25}_{-0.18}$	…	…
$\log_{10}(n_0/\mathrm{cm}^{-3})$	$2.79^{+0.50}_{-0.54}$	$-1.04^{+0.52}_{-0.48}$	$1.66^{+1.22}_{-1.80}$
p	$2.01^{+0.01}_{-0.01}$	$2.04^{+0.03}_{-0.02}$	$2.01^{+0.01}_{-0.01}$
$\log_{10}\epsilon_e$	$-0.25^{+0.18}_{-0.39}$	$-0.30^{+0.21}_{-0.30}$	$-0.79^{+0.64}_{-1.35}$
$\log_{10}\epsilon_B$	$-4.78^{+0.32}_{-0.16}$	$-2.28^{+1.14}_{-1.39}$	$-4.49^{+1.02}_{-0.40}$
ξ_N	$0.64^{+0.25}_{-0.28}$	$0.26^{+0.20}_{-0.12}$	$0.59^{+0.28}_{-0.31}$
$\log_{10}\Gamma_0$	$2.28^{+0.45}_{-0.36}$	$2.90^{+0.07}_{-0.09}$	∞
η_γ	$<21.0\%-59.4\%$	$<4.4\%-39.5\%$	$<0.7\%-46.9\%$
χ^2/DoF	16.9	10.4[a]	12.4
$\widehat{\mathrm{elpd}}$	6.4 ± 34.1	34.2 ± 22.4	21.2 ± 26.5

Note. We calculate η_γ using the 1σ distribution of $E_{K,iso}$ and the $E_{\gamma,iso}$ limits from Table 4. We present the $\widehat{\mathrm{elpd}}$ and minimum χ^2/DoF over 5000 posterior samples. We ran with 64 walkers and 75,000 iterations; we discarded 25,000.
[a] Although this is the smallest χ^2 of all AT 2021any configurations shown in this work, the top hat with ICC model underestimates the X-ray by $\sim 1/2$ an order of magnitude; the smaller χ^2 is likely because this model has a slightly better agreement with *X*-band (9.0–9.7 GHz) observations.

Table 20
Final Parameters (68% Uncertainty) for Selected Configurations of AT 2021lfa

Parameter	Gaussian ($\Gamma_0 = \infty$)	Top Hat (ICC)
t_0 [MJD]	$59337.19^{+0.19}_{-0.17}$	$59338.06^{+0.01}_{-0.01}$
θ_v [rad	$0.20^{+0.01}_{-0.01}$	$0.05^{+0.00}_{-0.00}$
$\log_{10}(E_{K,iso}/\mathrm{erg})$	$54.95^{+0.20}_{-0.31}$	$52.66^{+0.42}_{-0.28}$
θ_c [rad]	$0.02^{+0.01}_{-0.00}$	$0.12^{+0.01}_{-0.01}$
θ_w	$0.10^{+0.05}_{-0.05}$	…
$\log_{10}(n_0/\mathrm{cm}^{-3})$	$5.14^{+0.25}_{-0.33}$	$-0.52^{+0.38}_{-0.27}$
p	$2.13^{+0.05}_{-0.04}$	$2.64^{+0.05}_{-0.05}$
$\log_{10}\epsilon_e$	$-0.14^{+0.10}_{-0.17}$	$-0.56^{+0.21}_{-0.37}$
$\log_{10}\epsilon_B$	$-4.71^{+0.26}_{-0.20}$	$-1.88^{+0.57}_{-0.69}$
ξ_N	$0.02^{+0.01}_{-0.01}$	$0.55^{+0.30}_{-0.31}$
$\log_{10}\Gamma_0$	∞	$1.34^{+0.03}_{-0.02}$
η_γ	$<0.01\%-0.03\%$	$<1.0\%-4.8\%$
χ^2/DoF	5.4	4.5
$\widehat{\mathrm{elpd}}$	$(-1.0 \pm 0.3) \times 10^2$	$(1.3 \pm 0.2) \times 10^2$

Note. We calculate η_γ using the 1σ distribution of $E_{K,iso}$ and the $E_{\gamma,iso}$ limits from Table 4. We present the $\widehat{\mathrm{elpd}}$ and minimum χ^2/DoF over 5000 posterior samples. We ran with 64 walkers and 75,000 iterations; we discarded 25,000.

ORCID iDs

Maggie L. Li ⓘ https://orcid.org/0009-0001-6911-9144
Anna Y. Q. Ho ⓘ https://orcid.org/0000-0002-9017-3567
Geoffrey Ryan ⓘ https://orcid.org/0000-0001-9068-7157
Daniel A. Perley ⓘ https://orcid.org/0000-0001-8472-1996
Gavin P. Lamb ⓘ https://orcid.org/0000-0001-5169-4143
Nayana A.J. ⓘ https://orcid.org/0000-0002-8070-5400
Igor Andreoni ⓘ https://orcid.org/0000-0002-8977-1498
G. C. Anupama ⓘ https://orcid.org/0000-0003-3533-7183
Eric C. Bellm ⓘ https://orcid.org/0000-0001-8018-5348
Edo Berger ⓘ https://orcid.org/0000-0002-9392-9681
Joshua S. Bloom ⓘ https://orcid.org/0000-0002-7777-216X

Eric Burns ⓘ https://orcid.org/0000-0002-2942-3379
Ilaria Caiazzo ⓘ https://orcid.org/0000-0002-4770-5388
Poonam Chandra ⓘ https://orcid.org/0000-0002-0844-6563
Michael W. Coughlin ⓘ https://orcid.org/0000-0002-8262-2924
Kareem El-Badry ⓘ https://orcid.org/0000-0002-6871-1752
Matthew J. Graham ⓘ https://orcid.org/0000-0002-3168-0139
Mansi Kasliwal ⓘ https://orcid.org/0000-0002-5619-4938
Garrett K. Keating ⓘ https://orcid.org/0000-0002-3490-146X
S. R. Kulkarni ⓘ https://orcid.org/0000-0001-5390-8563
Harsh Kumar ⓘ https://orcid.org/0000-0003-0871-4641
Frank J. Masci ⓘ https://orcid.org/0000-0002-8532-9395

Richard A. Perley ⓘ https://orcid.org/0000-0001-7097-8360
Josiah Purdum ⓘ https://orcid.org/0000-0003-1227-3738
Ramprasad Rao ⓘ https://orcid.org/0000-0002-1407-7944
Antonio C. Rodriguez ⓘ https://orcid.org/0000-0003-4189-9668
Ben Rusholme ⓘ https://orcid.org/0000-0001-7648-4142
Nikhil Sarin ⓘ https://orcid.org/0000-0003-2700-1030
Jesper Sollerman ⓘ https://orcid.org/0000-0003-1546-6615
Gokul P. Srinivasaragavan ⓘ https://orcid.org/0000-0002-6428-2700
Vishwajeet Swain ⓘ https://orcid.org/0000-0002-7942-8477
Zachary Vanderbosch ⓘ https://orcid.org/0000-0002-0853-3464

References

Andreoni, I., Coughlin, M. W., Kool, E. C., et al. 2021, ApJ, 918, 63
Andreoni, I., Kumar, H., Coughlin, M., et al. 2023, GCN, 33229, 1
Aptekar, R. L., Frederiks, D. D., Golenetskii, S. V., et al. 1995, SSRv, 71, 265
Barniol Duran, R., Nakar, E., & Piran, T. 2013, ApJ, 772, 78
Barthelmy, S. D., Barbier, L. M., Cummings, J. R., et al. 2005, SSRv, 120, 143
Bellm, E. C., Kulkarni, S. R., Barlow, T., et al. 2019b, PASP, 131, 068003
Bellm, E. C., Kulkarni, S. R., Graham, M. J., et al. 2019a, PASP, 131, 018002
Beuermann, K., Hessman, F. V., Reinsch, K., et al. 1999, A&A, 352, L26
Burrows, D. N., Hill, J. E., Nousek, J. A., et al. 2005, SSRv, 120, 165
CASA Team, Bean, B., Bhatnagar, S., et al. 2022, PASP, 134, 114501
Cenko, S. B., Kulkarni, S. R., Horesh, A., et al. 2013, ApJ, 769, 130
Coughlin, M. W., Bloom, J. S., Nir, G., et al. 2023, ApJS, 267, 31
Cummings, J., Angelini, L., Barthelmy, S., et al. 2005, GCN, 3910, 1
Cunningham, V., Cenko, S. B., Ryan, G., et al. 2020, ApJ, 904, 166
de Ugarte Postigo, A., Malesani, D. B., Agui Fernandez, J. F., Thoene, C. C., & Geier, S. 2023, GCN, 34740, 1
Dekany, R., Smith, R. M., Riddle, R., et al. 2020, PASP, 132, 038001
Dermer, C. D., Chiang, J., & Bottcher, M. 1999, ApJ, 513, 656
Doe, S., Nguyen, D., & Stawarz, C. 2007, in ASP Conf. Ser. 376, Astronomical Data Analysis Software and Systems XVI, ed. R. A. Shaw, F. Hill, & D. J. Bell (San Francisco, CA: ASP), 543
Evans, P. A., Beardmore, A. P., & Page, K. L. 2007, A&A, 469, 379
Evans, P. A., Beardmore, A. P., & Page, K. L. 2009, MNRAS, 397, 1177
Foreman-Mackey, D., Hogg, D. W., Lang, D., & Goodman, J. 2013, PASP, 125, 306
Freeman, P., Doe, S., & Siemiginowska, A. 2001, Proc. SPIE, 4477, 76
Fruscione, A., McDowell, J. C., Allen, G. E., et al. 2006, Proc. SPIE, 6270, 62701V
Fulton, M. D., Smartt, S. J., Chen, T. W., et al. 2023, TNSAN, 179, 1
Galama, T. J., Frail, D. A., Sari, R., et al. 2003, ApJ, 585, 899
Garmire, G. P., Bautz, M. W., Ford, P. G., Nousek, J. A., & Ricker, G. R. J. 2003, Proc. SPIE, 4851, 28
Geng, J. J., Wu, X. F., Huang, Y. F., & Yu, Y. B. 2013, ApJ, 779, 28
Ghirlanda, G., Ghisellini, G., & Firmani, C. 2005, MNRAS: Letters, 361, L10
Ghirlanda, G., Nappo, F., Ghisellini, G., et al. 2018, A&A, 609, A112
Goldstein, A., Connaughton, V., Briggs, M. S., & Burns, E. 2016, ApJ, 818, 18
Gompertz, B., Ackley, K., Ramsay, G., et al. 2023, GCN, 34023, 1
Graham, M. J., Kulkarni, S. R., Bellm, E. C., et al. 2019, PASP, 131, 078001
Gupta, R., Kumar, A., Pandey, S. B., et al. 2022, JApA, 43, 11
Haislip, J. B., Nysewander, M. C., Reichart, D. E., et al. 2006, Natur, 440, 181
Hascoët, R., Beloborodov, A. M., Daigne, F., & Mochkovitch, R. 2014, ApJ, 782, 5
Heise, J., Zand, J. I. T., Kippen, R. M., & Woods, P. M. 2001, in Gamma-Ray Bursts in the Afterglow Era, ed. E. Costa, F. Frontera, & J. Hjorth (Berlin: Springer), 16
Hjorth, J., & Bloom, J. S. 2011, arXiv:1104.2274
Ho, A. Y. Q. 2023, GCN, 33238, 1
Ho, A. Y. Q., Perley, D. A., Beniamini, P., et al. 2020, ApJ, 905, 98
Ho, A. Y. Q., Perley, D. A., Yao, Y., et al. 2022, ApJ, 938, 85
Huang, Y. F., Cheng, K. S., & Gao, T. T. 2006, ApJ, 637, 873
Huang, Y. F., Dai, Z. G., & Lu, T. 2000, MNRAS, 316, 943
Huang, Y. F., Dai, Z. G., & Lu, T. 2002, MNRAS, 332, 735
Kobayashi, S., & Sari, R. 2000, ApJ, 542, 819
Kumar, H., Bhalerao, V., Anupama, G. C., et al. 2022, AJ, 164, 90
Kumar, P. 1999, ApJ, 523, L113

Kumar, P., & Zhang, B. 2015, PhR, 561, 1
Laskar, T., Alexander, K. D., Berger, E., et al. 2016, ApJ, 833, 88
Laskar, T., Berger, E., Tanvir, N., et al. 2013, ApJ, 781, 1
Law, N. M., Corbett, H., Galliher, N. W., et al. 2022, PASP, 134, 035003
Law, N. M., Kulkarni, S. R., Dekany, R. G., et al. 2009, PASP, 121, 1395
Lipunov, V., Kornilov, V., Zhirkov, K., et al. 2022, MNRAS, 516, 4980
Martin-Carrillo, A., Levan, A. J., de Ugarte Postigo, A., et al. 2023b, TNSCR, 2023-1961, 1
Martin-Carrillo, A., Schneider, B., Laskar, T., et al. 2023a, GCN, 34370, 1
Masci, F. J., Laher, R. R., Rusholme, B., et al. 2019, PASP, 131, 018003
Meegan, C., Lichti, G., Bhat, P. N., et al. 2009, ApJ, 702, 791
Mészáros, P. 2006, RPPh, 69, 2259
Nakar, E., & Piran, T. 2016, ApJ, 834, 28
Oke, J. B., Cohen, J. G., Carr, M., et al. 1995, PASP, 107, 375
Panaitescu, A., & Kumar, P. 2001, ApJ, 560, L49
Perley, D. A. 2019, PASP, 131, 084503
Perley, D. A. 2023, GCN, 33253, 1
Perley, D. A., Ho, A. Y. Q., Fausnaugh, M., et al. 2025, MNRAS, 537, 1
Perley, R. A., Chandler, C. J., Butler, B. J., & Wrobel, J. M. 2011, ApJL, 739, L1
Piran, T. 2005, RvMP, 76, 1143
Planck Collaboration, Aghanim, N., Akrami, Y., et al. 2020, A&A, 641, A6
Racusin, J. L., Oates, S. R., Schady, P., et al. 2011, ApJ, 738, 138
Rhoads, J. E. 1997, ApJL, 487, L1
Rhoads, J. E. 2003, ApJ, 591, 1097
Rhodes, L., Fender, R., Green, D., & Titterington, D. 2023, GCN, 34796, 1
Ridnaia, A., Frederiks, D., Lysenko, A., et al. 2023, GCN, 34051, 1
Roberts, O. J., Bala, S., Meegan, C. & Fermi GBM Team 2023, GCN, 34748, 1
Ruderman, M. 1975, in Seventh Texas Symposium on Relativistic Astrophysics, ed. P. G. Bergman, E. J. Fenyves, & L. Motz, Vol. 262 (New York: New York Academy of Sciences), 164
Ryan, G., Eerten, H., Piro, L., & Troja, E. 2020, ApJ, 896, 166
Sakamoto, T., Lamb, D. Q., Kawai, N., et al. 2005, ApJ, 629, 311
Salvaterra, R., Valle, M. D., Campana, S., et al. 2009, Natur, 461, 1258
Sarin, N., Hamburg, R., Burns, E., et al. 2022, MNRAS, 512, 1391
Schlafly, E. F., & Finkbeiner, D. P. 2011, ApJ, 737, 103
Schlegel, D. J., Finkbeiner, D. P., & Davis, M. 1998, ApJ, 500, 525
Schulze, S., Klose, S., Björnsson, G., et al. 2010, A&A, 526, A23
Sfaradi, I., Horesh, A., Rhodes, L., et al. 2023, TNSAN, 237, 1
Shvartzvald, Y., Waxman, E., Gal-Yam, A., et al. 2024, ApJ, 964, 74
Soderberg, A. M., Nakar, E., Cenko, S. B., et al. 2007, ApJ, 661, 982
Speagle, J. S. 2020, MNRAS, 493, 3132
Srinivasaragavan, G. P., Perley, D. A., Ho, A. Y. Q., et al. 2025, MNRAS, 538, 351
Steeghs, D., Galloway, D. K., Ackley, K., et al. 2022, MNRAS, 511, 2405
Steele, I. A., Smith, R. J., Rees, P. C., et al. 2022, Proc. SPIE, 5489, 679
Swain, V., Andreoni, I., Coughlin, M., Kumar, H., & Salgundi, A. 2023a, TNSAN, 178, 1
Swain, V., Andreoni, I., Coughlin, M., et al. 2023b, GCN, 34022, 1
Tagliaferri, G., Antonelli, L. A., Chincarini, G., et al. 2005, A&A, 443, L1
Tanvir, N. R., Fox, D. B., Levan, A. J., et al. 2009, Natur, 461, 1254
Tonry, J., Denneau, L., Weiland, H., et al. 2023, TNSCR, 2023-1419, 1
Tonry, J. L., Denneau, L., Heinze, A. N., et al. 2018, PASP, 130, 064505
Totani, T., & Panaitescu, A. 2002, ApJ, 576, 120
Vail, J., Li, M., Ho, A., et al. 2023a, GCN, 33934, 1
Vail, J. L., Li, M. L., Wise, J., et al. 2023b, GCN, 34730, 1
van der Walt, S., Crellin-Quick, A., & Bloom, J. 2019, JOSS, 4, 1247
van Eerten, H., Zhang, W., & MacFadyen, A. 2010, ApJ, 722, 235
Walker, M. A. 2001, MNRAS, 321, 176
Wang, K., Ho, A. Y. Q., Perley, D., & Transient Facility, Z. C. 2023, GCN, 33226, 1
Wang, L.-J., & Dai, Z.-G. 2013, ApJ, 774, L33
Watanabe, S. 2010, arXiv:1004.2316
Wu, X.-F., Gao, H., Ding, X., et al. 2013, ApJ, 781, L10
Xu, F., Geng, J.-J., Wang, X., Li, L., & Huang, Y.-F. 2022, MNRAS, 509, 4916
Xu, F., Huang, Y.-F., & Geng, J.-J. 2023, A&A, 679, A103
Ye, X.-M., Wei, D.-M., Zhu, Y.-M., & Jin, Z.-P. 2024, RAA, 24, 045011
Yi, S.-X., Lei, W.-H., Zhang, B., et al. 2017, JHEAp, 13-14, 1
Yuan, W., Zhang, C., Chen, Y., & Ling, Z. 2022, in Handbook of X-ray and Gamma-ray Astrophysics, ed. C. Bambi & A. Santangelo (Singapore: Springer), 1
Zeh, A., Klose, S., & Kann, D. A. 2006, ApJ, 637, 889
Zhang, B., & Mészáros, P. 2004, IJMPA, 19, 2385
Zhang, W., Woosley, S. E., & Heger, A. 2004, ApJ, 608, 365
Zhao, L., Liu, L., Gao, H., et al. 2020, ApJ, 896, 42